JOURNAL REVIEW

PDF Simulations of Ethylene Decomposition in Tubular LDPE Reactors

Nitin H. Kolhapure and Rodney O. Fox
Dept. of Chemical Engineering, Iowa State University, Ames, IA 50011

Andreas Daiβ
BASF AG, GCT/M-L544, 67056 Ludwigshafen, Germany

Frank-Olaf Mähling
Basell Polyolefine GmbH, M 510, 67056 Ludwigshafen, Germany

DOI 10.1002/aic.10378
Published online in Wiley InterScience (www.interscience.wiley.com).

The present study deals with turbulent reacting flow simulation inside low-density polyethylene (LDPE) tubular reactors, based on a detailed computational fluid dynamics (CFD) technique—transported probability density function (PDF) methods. The ability of the PDF methods to provide an exact representation of chemical source terms is ideally suited for coupling complex LDPE chemistry with small-scale fluid dynamic fluctuations in turbulent flow. LDPE chemistry with a total of 16 scalars provides an ideal test case for illustrating the applicability of an efficient chemistry algorithm based on in-situ adaptive tabulation. A particle-based Monte Carlo algorithm is used to solve the joint-composition PDF equation, whereas a finite-volume code is used to obtain hydrodynamic fields from the standard k–ε turbulence model. The influence of feed temperature, initiator concentration, and degree of premixing is investigated to gain detailed knowledge of micromixing effects on steady-state reactor performance. The computational approach provides a low-cost alternative to experimental and pilot-plant tests for exploring a variety of design options when making important design and operational decisions, or for investigating unstable reactor operating conditions. The ability of a simplified, but otherwise equivalent multi-environment-presumed PDF model to predict turbulence–chemistry interactions close to physical reality is validated using the detailed transported PDF simulations. The transported PDF method is shown to be an excellent tool for obtaining fundamental information on turbulent reacting flows, as well as for deriving simplified models for faster and easier interpretation of these flows when developing safe and efficient chemical processes. © 2005 American Institute of Chemical Engineers *AIChE J,* 51: 585–606, 2005

Keywords: CFD, micromixing, ethylene decomposition, LDPE reactor stability

Introduction

Turbulent reacting flows form an important class of problems with many applications in the chemical process industry. These flows are often characterized by interactions between the disparate range of length and time scales associated with chemical reactions and turbulent transport processes. The accurate modeling and simulation of turbulent reacting flows is still not fully mastered mainly because of the complexity and the coupling between fluid dynamics and chemistry at the microscale. Macroscopic reactor models such as continuous stirred tank reactors, plug-flow reactors, or batch reactors fail to capture subgrid-scale micromixing phenomena and the complex turbulence–chemistry interactions attributed to the idealized flow

Correspondence concerning this article should be addressed to N. H. Kolhapure at this current address: DuPont Engineering Research and Technology, 1007 N. Market St, Wilmington, DE 19898-0001; e-mail: nitin.h.kolhapure@usa.dupont.com.
F.-O. Mähling is currently at BASF AG., EVF/BP-H625, 67056 Ludwigshafen, Germany.

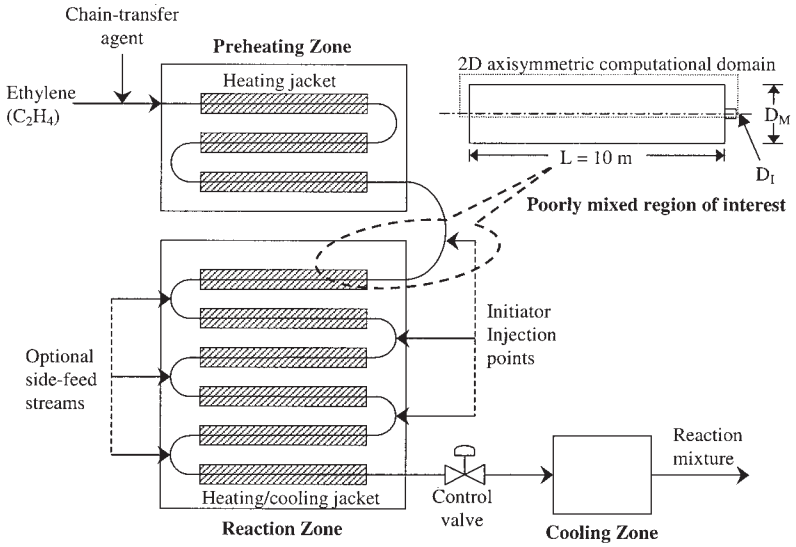

Figure 1. Tubular LDPE reactor and the poorly mixed region (L = 10 m) modeled in this work.

description. The complex interactions play a crucial role in determining reactant consumption, product selectivity, and reactor stability in processes that involve fast chemical reactions. Widespread examples of such mixing-sensitive chemical engineering processes include methane thermochlorination,[1-3] isobutylene polymerization,[4] anionic polymerization of methyl methacrylate,[5] ethylene free-radical polymerization,[6-9] fast crystallization,[10] reactive precipitation,[11,12] and nitration of benzene and toluene.[13]

In this study, we investigate the capability of a state-of-the-art CFD technique, namely, transported probability density function (PDF) methods, to predict complex turbulence–chemistry interactions in reacting flows with detailed chemistry using a representative industrial problem of engineering interest. Our example problem is the production of low-density polyethylene (LDPE), a commodity polymer with capacity of almost 18 million tons per year in 1996, which accounts for nearly 40% of global polyethylene production.[14] LDPE is exclusively produced by high-pressure free-radical polymerization in tubular or autoclave reactors. A schematic diagram of an industrial tubular LDPE reactor is shown in Figure 1. It consists of typically three zones: I. preheating zone; II. reaction zone; and III. cooling zone. The incoming monomer (that is, ethylene) is preheated to decompose the peroxide initiator, thereby starting polymerization in the reaction zone. This route accounts for almost 50% of total LDPE capacity, and is of increasing industrial importance as a result of commercial competition. The reactor line, which consists of the long narrow-jacketed spiral metallic pipe of 40–60 mm diameter and up to 1500 m in length, forms the heart of the LDPE production process and poses unique engineering challenges for the control of reaction conditions and optimization of reactors.

The essential lack of micromixing between initiator and ethylene close to the injection point creates a highly active reaction zone and decomposes the initiator prematurely. Because initiator costs are significant in total operating costs,[15] optimal process conditions are needed to achieve the efficient and cost-effective use of initiator. The nonuniform consumption of initiator also leads to undesired sustained temperature fluctuations, which can autoignite runaway ethylene decomposition reactions, resulting in unsafe reactor operations.[6,7,9,16,17] The phenomenon is typically termed as local or global "decomp" depending on the decomposition scale. A comprehensive knowledge of "decomp" events under various micromixing conditions will be useful for ensuring the safe operation of the reactor while controlling the polymer quality and downstream operations.[18-20] In light of these arguments, the objectives of the study reported herein are threefold:

(1) To apply the transported PDF method to better understand turbulence–chemistry interactions in the tubular LDPE reactor. Detailed transported PDF simulations are carried out to predict fundamental flow information at the micro-scale and hence, to investigate the reactor performance under various operating and mixing conditions. The capabilities of transported PDF methods are exploited to include detailed kinetics to obtain useful information regarding the loss of initiator and deterioration of polymer molecular properties for different feed temperatures. The investigations are extended to clarify the influence of different parameters, such as ethylene feed temperature, initiator concentration, and initiator feed pulsation on the occurrence of local and global decomposition events.

(2) To study the applicability of the recent chemistry algorithm, in-situ adaptive tabulation (ISAT),[21] for efficient chemistry calculations during detailed reacting flow simulations with the large number of chemical species and temperature involved in the complex LDPE chemistry.

(3) To validate the simplified multi-environment presumed PDF approach to predict turbulent reacting flows close to physical reality.[22] The simplified approach was successfully implemented for the LDPE process by Kolhapure and Fox.[7,23] The high computational efficiency of presumed PDF methods is extremely useful for sophisticated process design and analysis, which is otherwise not possible because of the high computational demands of transported PDF methods. For example, we can create reactor stability maps to develop safe operation strategies or to quantify loss of initiator for optimizing the reactor performance. Thus, the presumed PDF predictions are evaluated against transported PDF simulations to test

their accuracy and to increase their applicability for design and analysis of chemical processes.

Transported PDF Methods

A detailed introduction to computational models for turbulent reacting flows can be found in Fox.[24] In transported PDF methods, a statistical description of reacting flows is founded on the one-point joint PDF of the fluctuations of all concentrations and temperature (hereinafter referred to as the *composition*). The one-point joint composition PDF $f_\phi(\boldsymbol{\psi}; \boldsymbol{x}, t)$ is defined in terms of the probability of observing the event where the composition random fields at point $\boldsymbol{x}$ and time t fall in the differential neighborhood of fixed values $\boldsymbol{\psi}$:

$$f_\phi(\boldsymbol{\psi}; \boldsymbol{x}, t)d\boldsymbol{\psi} = \text{Prob}[\boldsymbol{\psi} < \boldsymbol{\phi}(\boldsymbol{x}, t) \leqslant \boldsymbol{\psi} + d\boldsymbol{\psi}] \tag{1}$$

PDF methods are generally classified as either "presumed" or "transported" depending on what assumptions are made concerning the joint PDF $f_\phi(\boldsymbol{\psi}; \boldsymbol{x}, t)$. Presumed PDF methods approximate the shape of the joint PDF, generally as a beta-PDF or a set of delta functions. Transported PDF methods do not require *a priori* knowledge of the joint PDF because the shape is computed from its transport equation. However, modeling of the unclosed molecular diffusion term to quantify the effect of micromixing on the shape of the joint PDF is nontrivial.

In either case, the principal advantage of the stochastic description is that the PDF can be defined in any turbulent reacting flow with exact treatment (that is, without closure) of any arbitrarily complex chemistry.[9] The transport equation for the one-point joint composition PDF is given as

$$\frac{\partial f_\phi}{\partial t} + \langle U_i \rangle \frac{\partial f_\phi}{\partial x_i} + \frac{\partial}{\partial x_i}[\langle u_i | \boldsymbol{\psi} \rangle f_\phi] = -\frac{\partial}{\partial \psi_\alpha}[\langle D_\alpha \nabla^2 \phi_\alpha | \boldsymbol{\psi} \rangle f_\phi] - \frac{\partial}{\partial \psi_\alpha}[S_\alpha(\boldsymbol{\psi}) f_\phi] \tag{2}$$

where $U_i = \langle U_i \rangle + u_i$. The terms on the left-hand side of Eq. 2 represent, respectively, the change in time of the PDF, convective transport in physical space arising from the mean velocity field (macromixing), and convective transport arising from the scalar-conditioned velocity fluctuations (mesomixing). On the righthand side of Eq. 2, the unclosed terms representing transport in composition space arising from molecular mixing and chemical reactions, respectively, can be identified.

A gradient-diffusion model[24,25] is used to close the term formed by convective transport arising from the scalar-conditioned velocity fluctuations:

$$\langle u_i | \boldsymbol{\psi} \rangle = -\frac{D_T}{f_\phi} \frac{\partial f_\phi}{\partial x_i} \tag{3}$$

This model then generates a "turbulent-diffusion" term in the composition PDF transport equation. The micromixing term is closed by the interaction-by-exchange-with-the-mean (IEM) model,[26] which assumes a linear relaxation of the scalar toward its mean value

$$\langle D_\alpha \nabla^2 \phi_\alpha | \boldsymbol{\psi} \rangle = \frac{1}{\tau_\phi}(\langle \phi_\alpha \rangle - \psi_\alpha) \tag{4}$$

where $\langle \phi_\alpha \rangle(\boldsymbol{x}, t)$ is the local scalar mean and τ_ϕ is the local micromixing time found from a separate model for the scalar dissipation rate. A detailed overview of the PDF method and the models for closing various terms involved in the transport equation are discussed in Fox[24] and Pope.[27] Transported PDF methods are the most computationally demanding. The transport equation contains a large number of independent variables and cannot be solved using standard discretization methods such as finite-difference or finite-element methods. A Monte-Carlo algorithm is an interesting alternative to obtain a computationally tractable solution. The main advantage of the algorithm is to realistically handle the complex chemistry by regarding each particle individually, depending on its properties and mass fractions.

The details of the Monte-Carlo algorithm and the simulation procedure are explained in Fox[24] and Tsai and Fox.[28] Here, the composition PDF is expressed in terms of a large number of notional particles (typically, 100–1000 in each grid cell) to cover the entire computational domain for an accurate estimation of the mean fields

$$\langle \boldsymbol{\phi} \rangle = \frac{1}{\mathbf{N}} \sum_{\mathbf{j=1}}^{\mathbf{N}} \boldsymbol{\phi}^{(j)} \tag{5}$$

where $\boldsymbol{\phi}^{(j)}$ is the chemical composition vector for jth particle. These particles obey a set of well-defined stochastic differential equations (SDE) corresponding to Eq. 2. Thus, the SDE for the jth particle in real and composition space evolves as

$$\frac{d\boldsymbol{x}^{(j)}}{dt} = \mathbf{C}^{(j)}(\boldsymbol{x}, t) + \mathbf{D}^{(j)}(\boldsymbol{x}, t) \tag{6}$$

$$\frac{d\boldsymbol{\phi}^{(j)}(t)}{dt} = \mathbf{M}^{(j)}(t) + \mathbf{S}[\boldsymbol{\phi}^{(j)}(t)] \tag{7}$$

where the superscript (j) indicates the jth particle, and $\mathbf{S}[\boldsymbol{\phi}^{(j)}(t)]$ is the chemical source term computed from the set of ordinary differential equations in the kinetic model. Other terms represent various transport processes: $\mathbf{M}^{(j)}(t)$ represents the molecular mixing process, whereas $\mathbf{C}^{(j)}(\boldsymbol{x}, t)$ and $\mathbf{D}^{(j)}(\boldsymbol{x}, t)$ represent the convection arising from mean velocity and turbulent diffusion, respectively.

Fractional time-stepping formulation

The chemical time scales involved in LDPE chemistry are smaller than the maximum transport time scale. Therefore, a fractional time-stepping method is used, which handles chemistry and transport processes separately and subsequently in one time step.[27] At each time step, the transport and chemical reaction contributions to the accumulation term are calculated using two different operators for real and composition space. The fractional time-stepping formulation involves the following steps to update the SDE for the jth particle:

(1) The position, velocity, and mean fields for each particle

are initialized using a linear spline interpolator and the initial conditions at the grid node (velocity, k, ε, pressure, species, and temperature fields).

(2) The position and velocity for the jth particle are updated according to Eq. 6. The equation is rewritten in the form of Langevin equation, using a random walk in real space, as

$$d\boldsymbol{x}^{(j)} = [\mathbf{C}^{(j)}(\boldsymbol{x}, t) + \mathbf{D}_1^{(j)}(\boldsymbol{x}, t)]dt + \mathbf{D}_2^{(j)}(\boldsymbol{x}, t)d\boldsymbol{W}(t) \quad (8)$$

where $\mathbf{C}^{(j)}(\boldsymbol{x}, t)$ is the mean velocity. $\mathbf{D}_1^{(j)}(\boldsymbol{x}, t)$ and $\mathbf{D}_2^{(j)}(\boldsymbol{x}, t)$ are derived by comparing Eq. 3 with the Reynolds averaged scalar transport equation.[9] The discretized version of Eq. 8 is expressed as

$$\boldsymbol{x}^{(j)}(t + \Delta t) = \boldsymbol{x}^{(j)}(t) + [\mathbf{C}^{(j)}(\boldsymbol{x}, t) + \mathbf{D}_1^{(j)}(\boldsymbol{x}, t)]_{\boldsymbol{x}^{(j)}(t)}\Delta t + [\mathbf{D}_2^{(j)}(\boldsymbol{x}, t)]_{\boldsymbol{x}^{(j)}(t)}\boldsymbol{\xi}\sqrt{\Delta t} \quad (9)$$

where $\boldsymbol{\xi}$ is a standardized joint normal random vector. The intermediate composition vector is then computed from $\boldsymbol{x}^{(j)}(t + \Delta t)$, $\boldsymbol{U}^{(j)}(t + \Delta t)$, and $\boldsymbol{\phi}^{(j)}(t)$, before chemistry takes place.

(3) Finally, the composition of the jth particle is updated according to Eq. 7 by using the fractional time-stepping procedure again.

- The composition vector is first updated for a full-time step using $\boldsymbol{\phi}^{(j)}$ at the initial time. The exact result from Eq. 4 is used to quantify the mixing term

$$\boldsymbol{\phi}^{\dagger(j)}(t) = \boldsymbol{\phi}^{(j)}(t) + \int_t^{t+\Delta t} \mathbf{M}^{(j)}(s)ds \quad (10)$$

- $\boldsymbol{\phi}^{\dagger(j)}(t)$ is then updated using the chemical source terms for the full-time step

$$\boldsymbol{\phi}^{(j)}(t + \Delta t) = \boldsymbol{\phi}^{\dagger(j)}(t) + \int_t^{t+\Delta t} \mathbf{S}[\boldsymbol{\phi}^{(j)}(s)]ds \quad (11)$$

At each time step, the total change for each particle is the simple sum of the individual changes arising from the transport and chemical operators. Thus, the transport processes do not have to be resolved using the small time steps that are required to resolve the chemical reactions more accurately, leading to the computationally efficient solution.

Detailed LDPE Chemistry

The transported PDF approach with chemical look-up tables for chemistry calculations has proved to be efficient for providing a detailed knowledge of the reacting flows in plant-scale tubular LDPE reactors.[9] It accounts for the stiff and nonlinear reaction mechanisms exactly, although the large computer memory requirement for *a priori* storage of chemical rates restricts its use to limited number of species. The basic chemistry used in our previous work was deceptively simple, requiring little more than an appropriate source of free radicals and chain transfer to monomer. It accounts for all reactions that involve monomer consumption and, hence, is sufficient to predict the effect of micromixing on yield. However, selectivity and the nature of the polymer are governed by the presence of chain-transfer agents as well as numerous competing side reactions that result in branching and premature chain termination. Inclusion of these side reactions with disparate timescales make the LDPE chemistry more complex (that is, a greater number of reactions and species), but represents the kinetics closer to physical reality. In light of these comments, a complex ethylene polymerization chemistry is used here to model chemical reactions. The reaction mechanism includes[29,30]: chain initiation (thermal as well as decomposition of various initiators such as organic peroxides or oxygen), chain propagation, chain transfer (to monomer, polymer, and chain-transfer agent), chain termination (combination as well as disproportionation), and other side reactions (intramolecular transfer to polymer, formation/propagation/β-scission of secondary radicals), which result in chain branches such as short-/long-chain branches (SCB/LCB) or double bonds (DB). These free-radical chain reactions are stoichiometrically represented in Table 1.

Table 1. Comprehensive Ethylene Polymerization Chemistry

Chain initiation		
Organic peroxide	$\mathrm{I}_{ni} \xrightarrow{f_{ni}, k_{d_{ni}}} 2\mathrm{A}_{ni}$	(ni = 1, 2)
or Azo compounds	$\mathrm{A}_{ni} + \mathrm{M} \xrightarrow{k_{i_1}} \mathrm{R}_1$	
Chain propagation		
	$\mathrm{M} + \mathrm{R}_i \xrightarrow{k_p} \mathrm{R}_{i+1}$	
Chain termination		
Combination	$\mathrm{R}_i + \mathrm{R}_j \xrightarrow{k_{tc}} \mathrm{P}_{i+j}$	
Disproportionation	$\mathrm{R}_i + \mathrm{R}_j \xrightarrow{k_{td}} \mathrm{P}_i^{=} + \mathrm{P}_j$	(DB)
Chain transfer		
To monomer	$\mathrm{M} + \mathrm{R}_i \xrightarrow{k_{trm}} \mathrm{P}_i^{=} + \mathrm{R}_1$	(DB)
To CTA	$\mathrm{CTA} + \mathrm{R}_i \xrightarrow{k_{cta}} \mathrm{P}_i + \mathrm{R}_{CTA}$	
To polymer	$\mathrm{R}_i + \mathrm{P}_j \xrightarrow{k_{trp}} \mathrm{P}_i + \mathrm{R}'_j$	
Chain branching		
SCB (backbiting)	$\mathrm{R}_i \xrightarrow{k_{SCB}} \mathrm{R}_i$	(SCB)
LCB	$\mathrm{M} + \mathrm{R}'_i \xrightarrow{k_{LCB}} \mathrm{R}_{i+1}$	(LCB)
β-scission	$\mathrm{R}'_{i+j} \xrightarrow{k_\beta} \mathrm{R}_i + \mathrm{P}_j^{=}$	(DB)

The complexity of the chemistry is further intensified by addition of simplified ethylene decomposition, which is necessary to evolve any criteria for the safe operation of the reactor by avoiding "decomp" events.[17,31,32] The mechanism includes important reactions such as initiation, propagation, and termination steps to produce major decomp products (C, CH_4, C_2H_2, and C_2H_6), shown in Table 2. These reactions are highly exothermic and autoaccelerating, thereby resulting in runaway conditions by developing high temperature and pressure inside the reactor. Albert[31] investigated the induction time required for explosive thermal decomposition of ethylene under high pressure and clearly marked the regions of polymerization as well as decomposition under various operating temperatures and pressures. The decomp events typically start at around 300°C when the operating pressure is >1500 atm and leads to explosion when temperatures are >350°C for stirred vessels. Most of the open literature on modeling the LDPE process mainly deals with polymerization chemistry and ignores the

Table 2. Simplified Ethylene Decomposition Chemistry*

Initiation	$2M \xrightarrow{k_1} C_2H_3^{\bullet} + C_2H_5^{\bullet}$
Propagation	$C_2H_5^{\bullet} \xleftrightarrow{k_2,k_2'} M + H^{\bullet}$
	$C_2H_5^{\bullet} + M \xrightarrow{k_3} C_2H_6 + C_2H_3^{\bullet}$
	$H^{\bullet} + M \xrightarrow{k_4} H_2 + C_2H_3^{\bullet}$
	$C_2H_3^{\bullet} \xrightarrow{k_5} C + CH_3^{\bullet}$
	$CH_3^{\bullet} + M \xrightarrow{k_6} CH_4 + C_2H_3^{\bullet}$
Termination	$CH_3^{\bullet} + CH_3^{\bullet} \xrightarrow{k_7} C_2H_6$
	$C_2H_3^{\bullet} + CH_3^{\bullet} \xrightarrow{k_8} C_2H_2 + CH_4$
	$C_2H_3^{\bullet} + C_2H_3^{\bullet} \xrightarrow{k_9} C_2H_2 + M$

*Zhang et al.[17]

decomposition reaction in spite of its importance in the overall process,[17] thereby limiting the usefulness of the model in process design, optimization, and control.

Starting from this comprehensive kinetic scheme, the chemical source terms are modeled based on the conservation of macromolecular species and energy.[17,29,30,32] The various composition variables in the polymerizing medium are described below:

- Concentrations of classical chemical species such as initiator, monomer, chain-transfer agent, various free radicals, dead polymer, and decomposition products
- Concentrations of pseudo-components: moments of the MWD, long- and short-chain branching frequencies, and double bonds
- Temperature of the reaction mixture

The treatment of free radicals results in an infinite set of composition variable corresponding to each radical with chain length distributed from one to infinity. To formulate a practical kinetic model, the method of moments is used to statistically describe the properties of free radicals and dead polymer chains. Moments of the free radical (μ), the secondary radical (ω), and the dead polymer (λ) are defined as[29]

$$\mu_n = \sum_{i=1}^{\infty} i^n [R_i] \tag{12}$$

$$\omega_n = \sum_{i=1}^{\infty} i^n [R_i'] \tag{13}$$

$$\lambda_n = \sum_{i=1}^{\infty} i^n [P_i] \tag{14}$$

where $[R_i]$, $[R_i']$, and $[P_i]$ denote the concentration of the free radical R_i, the secondary radical R_i', and the dead polymer P_i, respectively. The corresponding zeroth-order moment rate expressions are found by summing the expression of variation of chains with length i and then by multiplying each term by i and i^2 to obtain first- and second-order moment rate expressions. The dependency of second-order moment on the third-order moment is approximated using a truncated (after the first term) series of Laguerre polynomials with a gamma distribution weighting function[33]

$$\Lambda_3 = \frac{\Lambda_2}{\Lambda_1 \Lambda_0}(2\Lambda_2\Lambda_0 - \Lambda_1^2); \qquad \Lambda = \mu, \lambda, \omega \tag{15}$$

Overall, the comprehensive kinetic model involves a total of 28 composition variables, and is highly stiff in nature because of the wide range of chemical time scales associated with reactions. Estimation of the chemical source term in Eq. 11 is inherently computationally intensive because of high costs associated with the stiff numerical integrator. One approach to increase the computational throughput without the loss of accuracy is to substantially reduce the number of species, from 28 to 16, by invoking a quasi-steady-state approximation (QSSA) for free radicals. Previous studies have shown that such an approximation is valid for LDPE chemistry.[9,34] The chemical source terms for the 16 composition variables and QSSA estimates of the 12 free radicals are given in Tables 3 and 4, respectively.

The kinetic rate constants are expressed in generalized Arrhenius form (see Table 5). Estimation of ethylene polymerization kinetic rate constants by a number of researchers is compiled in Kiparissides et al.[29] However, the data in the literature for these rate constants vary over a wide range because of the complexity of the reaction mechanism with a large number of kinetic constants and different experimental conditions used for the studies. Thus, in this study, they are obtained from plant-scale data from Basell Polyolefine GmbH (Ludwigshafen, Germany). Because of industrial significance of the data, the exact values of these kinetic parameters must remain proprietary. Nevertheless, an investigative study found that a set of rate constants reported by Goto et al.,[35] Buback and Sandmann,[36] Buback and Lendle,[37] and Lee and Marano[38] are most consistent with industrial conditions. Estimation of ethylene decomposition kinetic rate constants is discussed in detail by Zhang et al.,[17] and are implemented in this work. Consistent sets of rate constants for the detailed polymerization kinetic scheme and simplified ethylene decomposition chemistry are given as exponential functions of pressure and temperature in Table 5. The rate of propagation of secondary radicals as well as rate of consumption of initiator free radical A are assumed to be the same rate as that of propagation of free radicals (that is, $k_{I_1} = k_{I_2} = k_{LCB} = k_p$). The chain-transfer agent used in this study is *n*-hexane.

In-situ adaptive tabulation

A typical transported PDF simulation for the LDPE tubular reactor involves 10^5–10^6 particles with 3000–6000 time steps. Even with the reduced number of species, direct integration (DI) of chemistry terms for each particle at each time step using Eq. 11 present a computationally formidable problem and alternative chemistry algorithms need to be explored. The implementation of ISAT algorithms has proved to be a highly efficient tool for accurate chemistry calculations with reasonable computational costs[1-3] by replacing direct integration with less-expensive multi-linear interpolation. The details of the ISAT algorithm are described elsewhere.[3,21] ISAT improves the storage problem in look-up tables by tabulating only the

Table 3. Final Expressions for the 16 Chemical Source Terms

$$S_{I_1} = -k_{d_1}[I_1] \quad \text{(ME1)}$$

$$S_{I_2} = -k_{d_2}[I_2] \quad \text{(ME2)}$$

$$S_{O_2} = -k_r[RH][O_2] \quad \text{(ME3)}$$

$$S_{CTA} = -k_{cta}[CTA]\mu_0 \quad \text{(ME4)}$$

$$S_{\lambda_0} = \frac{1}{2}k_{tc}\mu_0\mu_0\ k_{td}\mu_0\mu_0 + k_{trm}[M]\mu_0 + k_{cta}[CTA]\mu_0 + k_\beta(\omega_1 - \omega_0) \quad \text{(ME5)}$$

$$S_{\lambda 1} = \frac{1}{2}k_{tc}(2\mu_0\mu_1) + k_{td}\mu_0\mu_1 + k_{trm}[M]\mu_1 + k_{cta}[CTA]\mu_1 + k_\beta\left(\frac{\omega_2 - \omega_1}{2}\right) + k_{trp}\lambda_1\mu_1 - k_{trp}\mu_0\lambda_2 \quad \text{(ME6)}$$

$$S_{\lambda_2} = \frac{1}{2}k_{tc}(2\mu_1\mu_1 + 2\mu_0\mu_2) + k_{td}\mu_0\mu_2 + k_{trm}[M]\mu_2 + k_{cta}[CTA]\mu_2 + k_\beta\left(\frac{2\omega_3 - 3\omega_2 + \omega_1}{6}\right) + k_{trp}\lambda_1\mu_2 - k_{trp}\mu_0\lambda_3 \quad \text{(ME7)}$$

$$S_{SCB} = k_{SCB}\mu_0 \quad \text{(ME8)}$$

$$S_{LCB} = k_{LCB}[M]\omega_0 \quad \text{(ME9)}$$

$$S_{DB} = k_{trm}[M]\mu_0 + k_\beta\omega_0 + k_{td}\mu_0\mu_0 \quad \text{(ME10)}$$

$$S_C = \frac{k_6}{\sqrt{k_t}}\sqrt{\frac{k_1}{2}}[M][M] \quad \text{(ME11)}$$

$$S_{CH_4} = \left(\frac{1}{2}k_1 + \frac{k_6}{\sqrt{k_t}}\sqrt{\frac{k_1}{2}}\right)[M][M] \quad \text{(ME12)}$$

$$S_{C_2H_6} = \frac{3}{2}k_1[M][M] \quad \text{(ME13)}$$

$$S_{C_2H_2} = k_1[M][M] \quad \text{(ME14)}$$

$$S_M = -(k_{I_1}[A_1] + k_{I_2}[A_2] + 2k_{th}[M]^2 + k_p\mu_0 + k_{trm}\mu_0 + k_{LCB}\omega_0)[M] - \left(\frac{3}{2}k_1 + \frac{k_6}{\sqrt{k_t}}\sqrt{\frac{k_1}{2}}\right)[M][M] \quad \text{(ME15)}$$

$$S_T = -\Delta H_{poly}(k_p[M]\mu_0 + k_{tc}\mu_0\mu_0 + k_{td}\mu_0\mu_0 + k_{I_1}[A_1][M] + k_{I_2}[A_2][M] + k_r[RH][O_2]) - \Delta H_{decomp}\left(1.5k_1 + \frac{k_6}{\sqrt{k_t}}\sqrt{2k_1}\right)[M][M] \quad \text{(ME16)}$$

accessed composition region of a given flow simulation, rather than the entire allowable composition space. Thus it does not require storage for unneeded compositions. The technique uses a common feature of chemical kinetics, namely, the large separation in chemical time scales (relative to flow scales), and the compactness of the accessed region, to reduce the computational efforts. Here the look-up table is generated during the course of flow simulation to store reaction information (for example, integrated reaction increment, temperature, and so on). Once the table is generated, direct integration of the chemical kinetic equations is replaced in the CFD simulation by a more efficient multi-linear interpolation. ISAT offers significant gains in computational efficiency, up to a factor of 100, without reducing the degrees of freedom of the detailed kinetic scheme.[3] A performance evaluation study for the algorithm was carried out using the transported PDF approach with LDPE chemistry and is reported below.

In general, kinetic and thermodynamic data are supplied to ISAT (ISAT-CK version 1.0) using the Chemkin II library. Input files (streams1.ldpe and chem.ldpe) describe the elementary reaction mechanisms in Chemkin format and are interpreted by a Fortran program (ckinterp.f) to generate a Chemkin input file (cklink), as shown in Figure 2. However, in this case, an external routine (usrate.f) is defined to include user-customized kinetic rate expressions (constants.f) as well as physical and thermodynamic constants (functions.f) for the detailed LDPE chemistry. The chemical source term is computed using numerical integration in early time steps and stored along with other records (chemical composition vector, time step, Jacobian matrix of the chemical source term for sensitivity analysis, and error control parameters) in a dynamically built look-up table. The table generated in ISAT has the form of a multi-dimensional binary tree. The position of the set of records is determined by the composition vector for the notional particles at each fractional time step, which are treated as query points in the multi-dimensional space.

A table entry starts with the first query point (determined by initial composition vector). For the subsequent query points, ISAT searches the table for a closest point to the query. If this closest point falls inside the *ellipsoid of accuracy* (EOA = a region of accuracy around the ISAT entry), then it performs multilinear interpolation to compute the chemical source term by retrieving the associated matrices at the closest point. This step is called a *retrieve*. If the new query point lies outside the

Table 4. QSSA Estimates of the 12 Free-Radical Species

$$[A_1] = \frac{2k_{d_{I_1}}[I_1]}{k_{I_1}[M]} \quad \text{(QE1)}$$

$$[A_2] = \frac{2k_{d_{I_2}}[I_2]}{k_{I_2}[M]} \quad \text{(QE2)}$$

$$\mu_0 = \frac{B + \sqrt{B + 4A(k_t c + k_t d)}}{2(k_t c + k_t d)} \quad \text{(QE3)}$$

where $B = k_{trp}\lambda_1 + k_{cta}[CTA]$

$$A = k_{I_1}[A_1][M] + k_{I_2}[A_2][M] + 2k_{th}[M]^3 + k_{LCB}[M]\omega_0 + k_\beta(\omega_1 - \omega_0)$$

$$\mu_1 = \frac{C}{D} \quad \text{(QE4)}$$

where $C = k_{I_1}[A_1][M] + k_{I_2}[A_2][M] + 2k_{th}[M]^3 + k_{trm}[M]\mu_0 + k_p[M]\mu_0 + k_{LCB}[M](\omega_1 + \omega_0) + \frac{1}{2}k_\beta(\omega_2 - \omega_1)$

$$D = k_{tc}\mu_0 + k_{td}\mu_0 + k_{trm}[M] + k_{trp}\lambda_1 + k_{cta}[CTA]$$

$$\mu_2 = \frac{E}{D} \quad \text{(QE5)}$$

where $E = k_{I_1}[A_1][M] + k_{I_2}[A_2][M] + 2k_{th}[M]^3 + k_{trm}[M]\mu_0 + k_p[M](2\mu_1 + \mu_0) + k_{LCB}[M](\omega_2 + 2\omega_1 + \omega_0) + k_\beta\left(\frac{2\omega_3 - 3\omega_2 + \omega_1}{6}\right)$

$$\omega_0 = \frac{k_{trp}\mu_0\lambda_1}{k_{LCB}[M] + k_\beta} \quad \text{(QE6)}$$

$$\omega_1 = \frac{k_{trp}\mu_0\lambda_2}{k_{LCB}[M] + k_\beta} \quad \text{(QE7)}$$

$$\omega_2 = \frac{k_{trp}\mu_0\lambda_3}{k_{LCB}[M] + k_\beta} \quad \text{(QE8)}$$

$$[C_2H_5^\bullet] = \frac{k_1[M][M](k_2' + k_4)}{k_2k_4 + k_2'k_3[M] + k_3k_4[M]} \quad \text{(QE9)}$$

$$[H^\bullet] = \frac{k_1k_2[M]}{k_2k_4 + k_2'k_3[M] + k_3k_4[M]} \quad \text{(QE10)}$$

$$[C_2H_3^\bullet] = \frac{[M]}{2}\sqrt{\frac{2k_1}{k_t}} \quad \text{(QE11)}$$

$$[CH_3^\bullet] = \frac{[M]}{2}\sqrt{\frac{2k_1}{k_t}} \quad \text{(QE12)}$$

region of accuracy, direct integration is performed at the new query point and is used to determine a local error ε against ISAT linear approximation. If query points are encountered for which the local error is less than user-supplied error tolerance ε_{tol} (set in opt.ldpe), the EOA for a query retrieval is expanded to include the new query point and a *growth* step occurs. However, if $\varepsilon > \varepsilon_{tol}$, then the query point is added as a new entry to the table, leading to an *addition* step. The output data files from ISAT (ci.op and tc.op) contain information on input chemistry, error control parameters, and performance parameters such as the number of records, CPU time, and so forth.

ε_{tol} Selection

The accuracy of chemical source terms computed using ISAT will have a strong dependency upon ε_{tol}. Smaller ε_{tol} values will increase the accuracy of simulations, but will also increase the number of records in the table. This will decrease the computational efficiency because addition of new entries to the table requires multiple integrations to compute the local error as well as the sensitivity matrices, and is the most expensive part of ISAT. Thus, selection of an appropriate value of ε_{tol} is crucial to achieve high computational efficiency with negligible loss of accuracy. Figures 3 and 4 show the radially averaged initiator (g_I), monomer (g_M), and carbon mass fractions (g_C), as well as temperature profiles, by implementing ISAT in transported PDF simulations for Case 1 and Case 2, respectively, in Table 6. The profiles are generated using ISAT for a fixed number of queries after steady-state solution with different values of ε_{tol}: 0.1, 0.01, and 0.001. In this case, 100 time steps of transported PDF simulations are carried out for 16 species after the steady-state solution at a given inlet conditions. The corresponding profiles using DI for the same number

Table 5. Kinetic Rate Constants

k	k_0* ($m^3\ mol^{-1}\ s^{-1}$)	E_a (J/mol)	V_a** (cm^3/mol)
$k_{d_{1\text{-}1}}$†	6.1×10^{14}	1.254×10^5	2.1
$k_{d_{1\text{-}2}}$††	5.69×10^{15}	1.477×10^5	8.7
$k_{d_{\beta}}$†	1.41×10^{15}	1.515×10^5	10.06
k_p‡	5.887×10^4	2.970×10^4	−22.96
k_{tc}‡	3.246×10^5	—	4.98
k_{td}‡	1.075×10^6	1.247×10^3	−14.03
k_{trm}‡	5.823×10^2	4.623×10^4	−19.99
k_{cta}‡	3.306×10^4	4.197×10^4	−19.99
k_{trp}‡	4.116×10^2	3.223×10^4	−19.99
k_{SCB}‡‡	1.56×10^6	5.452×10^4	−23.50
k_{β}‡‡	2.36×10^4	6.079×10^4	−18.46
k_1§	4.003×10^{16}	2.720×10^5	−7.999
$k_6/\sqrt{k_t}$§	1.587×10^{17}	2.720×10^5	13.29

Note: Rate constants are given as $k = k_0 \exp[-(E_a + V_a P_{atm})/RT]$.
*Units of k_0 for $k_{d_{1\text{-}1}}$ are 1/s.
**V_a can be expressed in terms of cal/atm · mol by using a conversion factor of 0.02422.
†Buback and Sandmann.[36]
††Buback and Lendle.[37]
‡Lee and Marano.[38]
‡‡Goto et al.[35]
§Zhang et al.[17]

of queries are obtained for the comparison. As seen in Figure 3, $\varepsilon_{tol} = 0.1$ gives fairly accurate results for g_I for Case 1. However, the best agreement between ISAT and DI for g_M, g_C, and temperature is observed with $\varepsilon_{tol} = 0.001$. Figure 4 shows that the predictions are much more sensitive to ε_{tol} values for Case 2, mainly because of the occurrence of global ethylene decomposition. The decomposition time scales are much smaller than polymerization time scales, and thus the computation of decomposition rate constants with larger ε_{tol} (0.1 and 0.01) introduces larger errors and leads to unrealistic predictions close to the point where decomposition occurs. For Case 2 or for unstable reactor operating conditions, adequate agreement between ISAT and DI is achieved with $\varepsilon_{tol} = 0.001$.

Efficiency and storage requirements of ISAT

The speed-up factor, which is the ratio of CPU time for DI to CPU time for ISAT using a fixed number of queries after steady-state solution, is used to evaluate the computational efficiency of ISAT. Transported PDF simulations were carried out on a Sun Ultra 80 workstation for 16 species using different T_{feed} values with total number of particles 126,720 and differ-

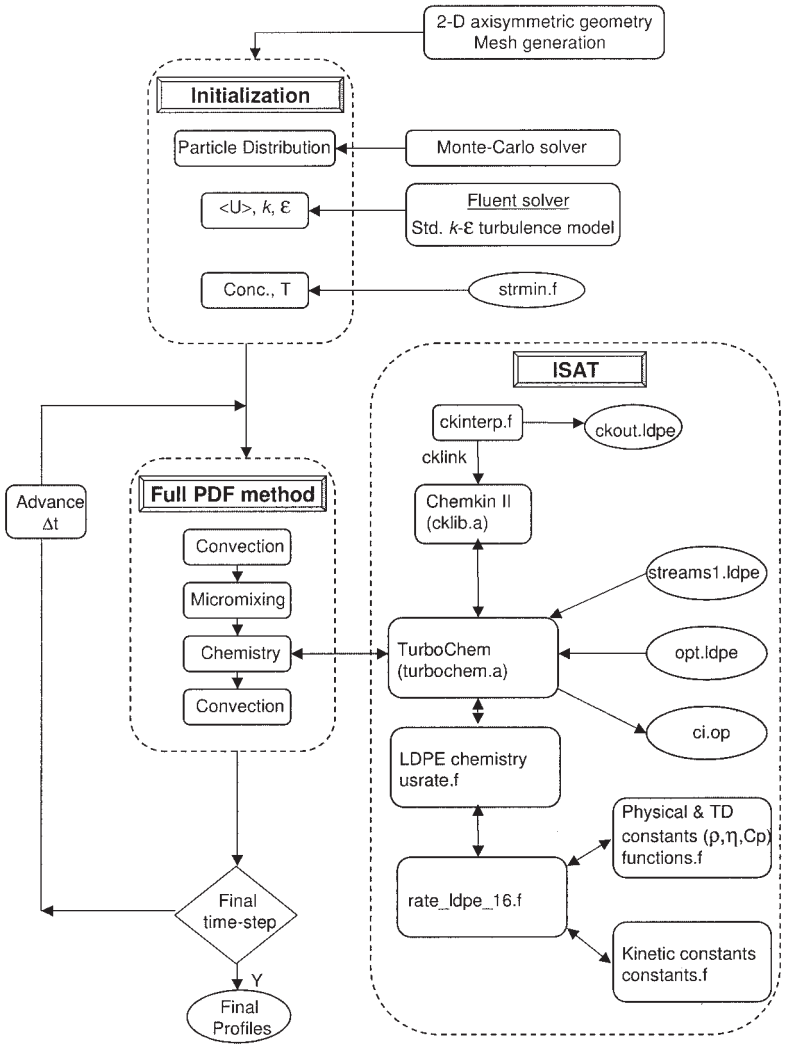

Figure 2. Simulation procedure for transported PDF simulation using Monte-Carlo and ISAT algorithms.

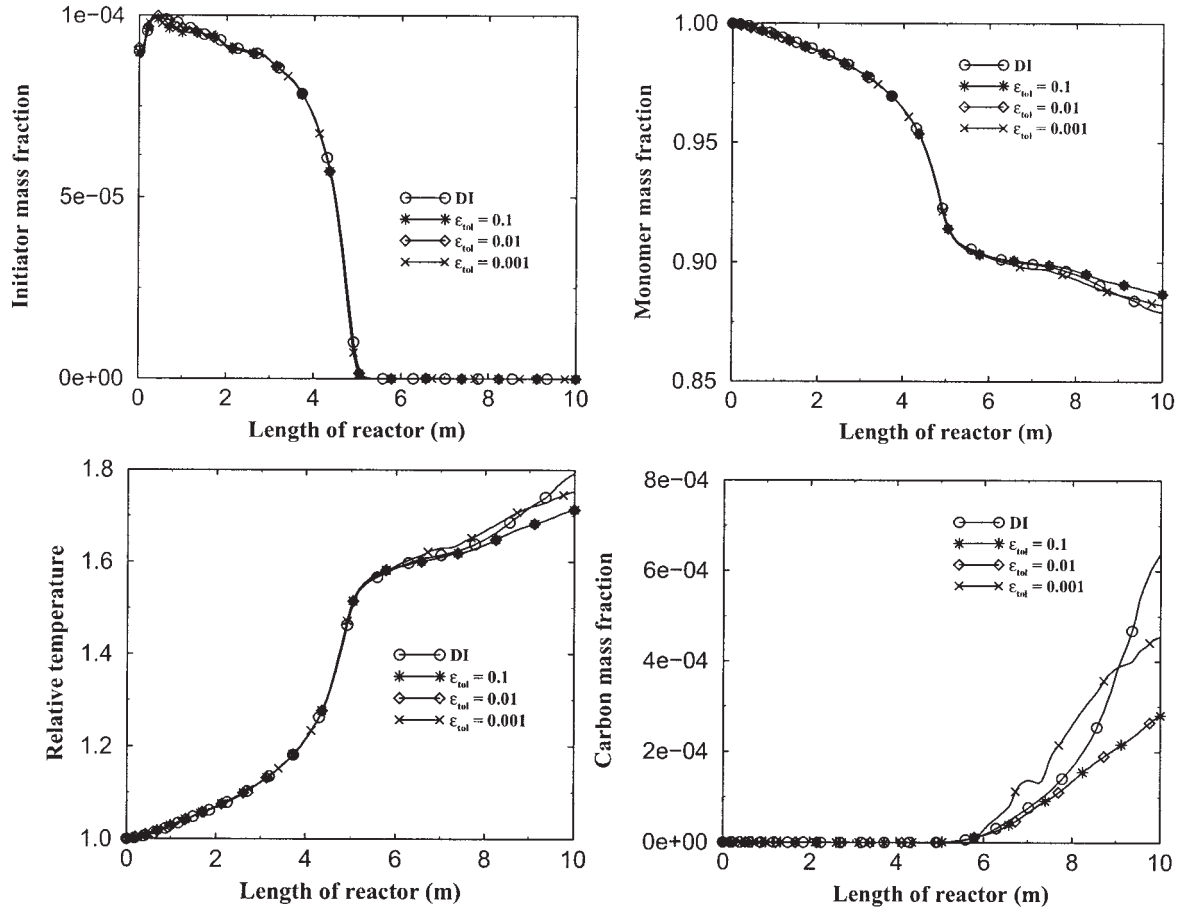

Figure 3. Effect of error tolerance on the prediction of radially-averaged axial species profiles for Case 1.

Top left: initiator mass fraction. Top right: monomer conversion. Bottom left: relative temperature. Bottom right: mass fraction of decomposition product, carbon. Note that $\varepsilon_{tol} = 0.001$ gives adequate agreement between ISAT and direct integration (DI) predictions.

ent ε_{tol} values. Table 6 shows that ISAT offered from 2 to 32 times computational gains compared to the conventional DI methods when used during transported PDF simulations for 100 time steps. With the coarsest error tolerance ($\varepsilon_{tol} = 0.1$), the EOA can grow, thereby increasing computational gains with a higher number of retrieves from the ISAT table. This is reflected in low number of records, that is, 68 and 88 for Case 1 and Case 2, respectively, in the table. It is observed that approximately 192 records are generated per MB of storage RAM used in the simulation for all ε_{tol} values. This number is helpful while calculating the corresponding memory requirement. With finer error tolerance ($\varepsilon_{tol} = 0.001$), the relatively smaller EOA requires a higher number of records, thereby increasing the CPU time and storage requirements. The number of records generated in the binary tree data structure increased from 257 to 47,613 when T_{feed} is increased from 225 to 250°C, which will require higher RAM to carry out simulations. This is mainly attributable to the wide range of chemical time scales involved in the decomposition chemistry. Thus, the total memory requirement to carry out transported PDF simulations with safe operating conditions is approximately 43 MB (8250 records) to achieve the observed speed-up factor. However, the memory requirement increases tremendously with decomposition conditions. The storage requirement can be decreased by using a restart file, which is obtained by storing all variables for all particles at intermediate time steps. The simulation is restarted at the intermediate time step to rebuild the ISAT table. The computational gains offered by ISAT make it possible to carry out transported PDF simulations for the stiff kinetic expressions involved in the complex LDPE chemistry. It also allows us to include all interrelated chemical reactions and their sensitivity to local diffusion fluxes, thereby predicting the micromixing effect on selectivity and local hot spots.

Simulation Procedure

The transported PDF simulation of the entire length of the reactor with multiple initiator injections would require formidable computational resources. We, therefore, restrict our attention to the mixing-sensitive reaction zone formed as a result of the first initiator injection and mixing-sensitive operating conditions such as high monomer feed temperatures or high initiator concentrations. Under such cases, chemical time scales are very small compared to micromixing and it is possible to use a smaller length of the reactor (such as 10 m, as shown in Figure 1) as a computational domain for steady-state simulation to investigate phenomena such as premature initiator decomposition or autoignition of ethylene decomposition. The radius of the computational domain is 19 mm.

Figure 2 gives an overview of the various steps involved in

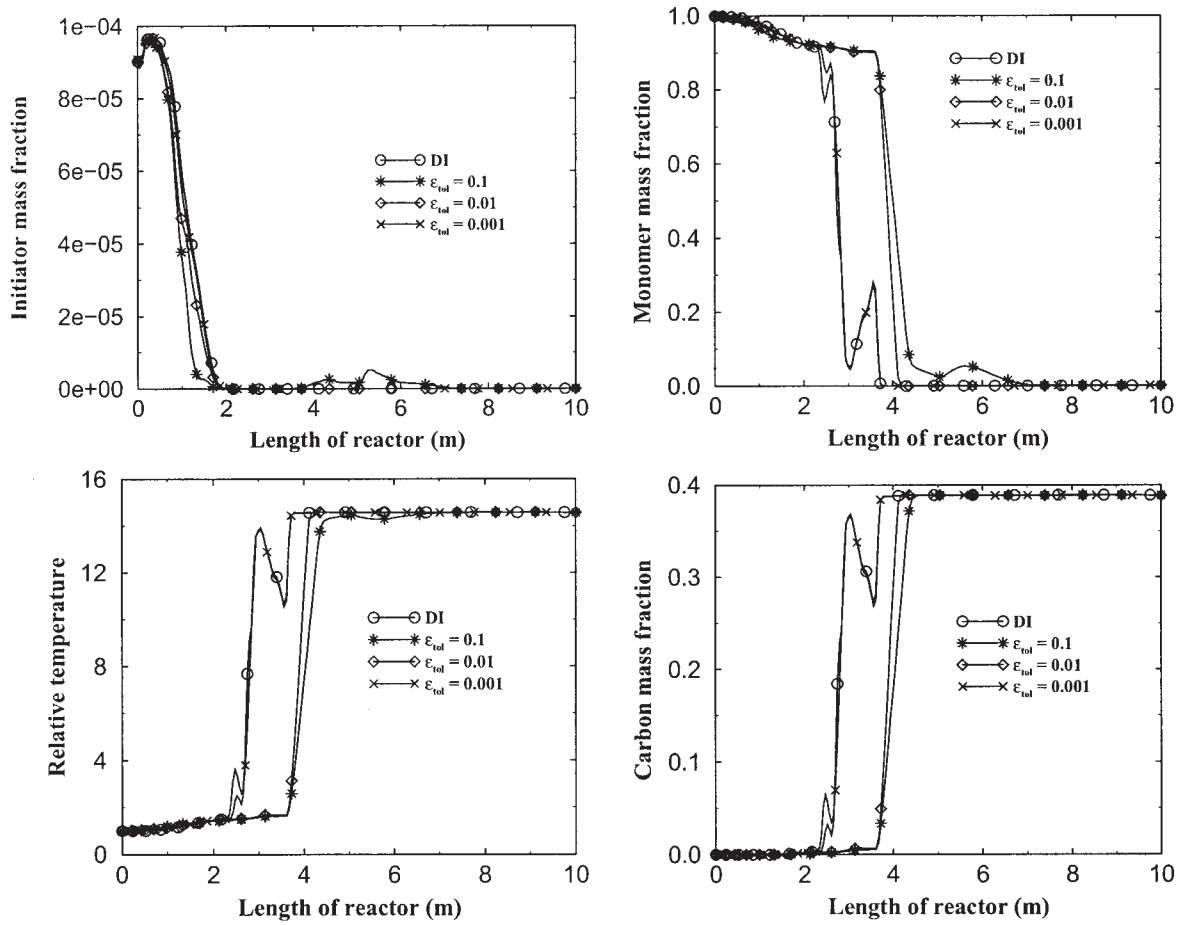

Figure 4. Effect of error tolerance on the prediction of radially-averaged axial species profiles for Case 2.

Top left: initiator mass fraction. Top right: monomer conversion. Bottom left: relative temperature. Bottom right: mass fraction of decomposition product, carbon. Note that $\varepsilon_{tol} = 0.001$ gives adequate agreement between ISAT and DI predictions.

transported PDF simulation using our in-house FORTRAN codes. The detailed simulation procedure is discussed by Tsai and Fox.[9,28] In the Monte-Carlo method, the composition PDF is expressed in terms of a large number of notional particles that are uniformly distributed in a two-dimensional, axisymmetric computational domain with 199 × 9 cells with a uniform grid spacing in the radial direction. We are using a denser grid in the first section of the reactor to explore the physical phenomena occurring near the initiator injection point. Negligible viscosity effects arising from fully developed monomer flow makes it possible to use the standard k–ε model to define turbulence. The Navier–Stokes equations and the standard k–ε equations are solved in Fluent® for the flow and hydrodynamic fields (velocity, k, ε, pressure) at each grid point in the computational domain. The transported PDF code is initialized by reading the steady-state solution of the flow field at each grid node from the output of Fluent®.[39] The averaged values of those quantities are linearly interpolated onto each notional particle according to its location in the computational domain. All inflow particles are initialized using pure monomer at the feed temperature except in the injection cells, where particles are premixed with initiator and monomer. Attention was given

Table 6. Performance Study for ISAT Using 100 Time Steps for Two-Dimensional Transported PDF Simulations at Various T_{feed}

Case	T_{feed} (°C)	Procedure	ε_{tol}	Records	Storage MB of RAM	CPU Time (h)	Speed-Up Factor
1	225	DI	—	—	—	10.28	—
		ISAT	0.1	68	0.35	0.65	15.82
		ISAT	0.01	84	0.44	0.87	11.82
		ISAT	0.001	257	1.34	0.87	11.82
2	250	DI	—	—	—	16.42	—
		ISAT	0.1	88	0.46	0.52	31.58
		ISAT	0.01	2153	11.20	1.41	11.65
		ISAT	0.001	47613	247.60	6.99	2.35

to various simplifications such as the fractional time-stepping approach, which would reduce computational intensity without compromising the physics of the flow. The flow field is kept constant once the solution is initialized. As the simulation proceeds, these particles move from cell to cell according to macromixing and mesomixing terms, mix within the cell according to micromixing terms, and react within the cell according to the well-defined chemical source term.

The simulation parameters for the plant-scale tubular reactor are identified based on their impact on the stability and optimal performance of the reactor. Critical values of these parameters are selected mainly to investigate the effect of micromixing in close proximity to the unsafe reactor operation. The description of key simulation parameters and their interrelation with the operating parameters is presented below.

(1) Monomer feed temperature, T_{feed}

The temperature of the reaction mixture at the first injection point is defined as monomer feed temperature. The general trend is to use the maximum possible T_{feed} to optimize the overall process. However, there is strong relation between extreme values of T_{feed} and the proximity to the safe operation of the reactor. This parameter is important to study the reactor performance in critical regions where instabilities occur. T_{feed} can be varied by changing the flow rate of coolant water in the feed preheating zone. Our investigation found that the reactor is particularly sensitive to decomposition in the T_{feed} range of 225–250°C. The two cases selected here (Table 6) for transported PDF simulations represent the lower and upper limits of this range. Temperature fields in this paper are scaled using T_{feed} values.

(2) Initiator concentration, g_I

Mass fraction of initiator at the inlet is another simulation parameter, which is directly related to the steady-state outlet temperature as well as the steady-state reactor length required for optimum performance. The parameter can be varied easily by changing the mass flow rate (g/h or mol/h) of initiator.

(3) Initiator feed pulsation

Pulsating feed occurs in plant-scale operation and increases g_I for intermittent time steps, making it a crucial parameter to investigate the reactor stability.

The degree of premixing ($p_{1,0}$) between initiator and monomer is controlled by varying the number of injection cells in the transported PDF simulations. $p_{1,0}$ represents the ratio of the area of the injection nozzle to the cross-sectional area of the tubular reactor at the inlet, assuming the same inlet velocities for initiator (I) and monomer (M) feed streams. In general, $p_{1,0}$ is defined as

$$p_{1,0} = \frac{Q_I}{Q_M + Q_I} = \frac{D_I^2 v_I}{D_M^2 v_M + D_I^2 v_I} \tag{16}$$

where Q, v, and D indicate volumetric flow rate (m^3/s), axial velocity (m/s), and diameter (m), respectively. Typically, center-mode injection ($p_{1,0}$ with $v_I = v_M$) is used in the plant-scale reactor and is selected for simulation studies. Mixing parameter C_ϕ determines the time required for completion of micromixing. In general, near-unit values of C_ϕ describe fully developed turbulent pipe flows, and $C_\phi = 1$ is used for simulations. The initiation is assumed to occur only because of peroxide initiators. The study uses three peroxide initiators, which are termed as low-temperature (I-1), medium-temperature (I-2), and high-temperature (I-3) initiators, depending on the temperature of activation. Each initiator has a specific temperature range of use, where its specific consumption is minimal.[40] The various physical and thermodynamical constants used in the simulation are given in Table 7.

Table 7. Physical Constants Used in the Simulation

P_{atm} (atm)	ρ* (kg/m^3)	$\langle U_z \rangle$ (m/s)	C_p* (J/kg · K)	ΔH_{poly}* (J/mol)	ΔH_{decomp}** (J/mol)
2,150	444	21.85	2,510	94,893	126,357

*Tsai and Fox.[9]
**Zhang et al.[17]

Results and Discussion

The transported PDF simulations are carried out with three objectives. First, the species and concentration distribution are investigated using the full LDPE chemistry, leading to a detailed description of stability and performance of the reactor under different operating conditions. Second, fundamental information about the interaction between mixing and chemistry at the micro-scale is obtained. Finally, a validation study of the presumed PDF approach is carried out to increase our confidence in using the simplified presumed PDF model for process design.

Investigation of reactor performance and stability

Species and Temperature Distributions. Typical transported PDF simulation results are presented in Figures 5 and 6 as an illustration of the micromixing process for Case 1, using a mixture of two initiators (I-1 and I-2) with inlet mass fractions equal to 2.37×10^{-5} and 4.14×10^{-5}, respectively. Center-mode initiator injection is used with two injection cells corresponding to $p_{1,0} = 6.25\%$. Other assumptions made during the simulation are constant initiator efficiency ($f = 0.624$ for I-1 and 1.0 for I-2). Figure 5 shows the variation in mean fields of monomer mass fraction (g_M), temperature, and initiator mass fractions ($g_{I\text{-}1}$ and $g_{I\text{-}2}$) inside the LDPE reactor. Surface plots of initiators in Figure 5 show that the center-mode injection of a small initiator stream creates sharp concentration gradients close to the injection point. Physically, the concentration space is segregated to form distinct reaction environments with very high local concentration of initiator near the point of injection. Because chemical reactions are very fast compared to micromixing, the reaction environments act like strong sinks to which monomer is supplied by a slow diffusion process, given that the reaction can take place only as fast as both initiator and monomer are supplied at the same location. The high initiator free radical activity in the reaction environments yields higher polymerization rates, leading to sudden release of energy locally. It also results in higher termination of initiator free radical, causing loss of initiator arising from quick burnout. The exact loss of initiator can be quantified in terms of initiator efficiency by comparing the transported PDF results for the radially-averaged initiator mass fraction profiles with that of the plug-flow reactor model. Such quantification will be extremely useful to predict the effect of poor mixing on the loss of initiator, and to decide the operating conditions for optimal use of the expensive initiators. Thus the

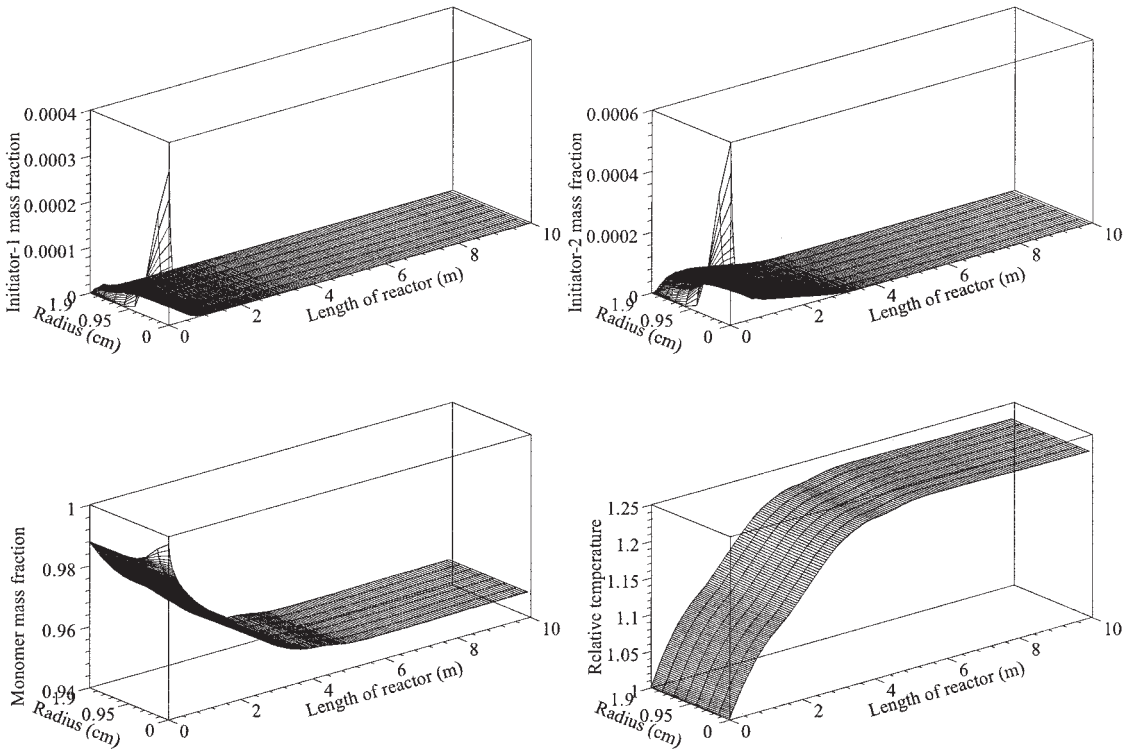

Figure 5. Time-averaged surface plots for $g_{I\text{-}1}$ (top left), $g_{I\text{-}2}$ (top right), g_M (bottom left), and relative temperature (bottom right) mean fields in the computational domain for Case 1.

local importance of micromixing increases when the large concentration and temperature fluctuations are created and mixing-sensitive reactions affect the reactor performance. Approximately 4.25% of monomer conversion is seen in the monomer mass fraction fields in the bottom left of Figure 5, whereas the bottom right of Figure 5 shows the corresponding increase in the temperature of the reaction mixture to a steady-state value of 275°C.

Figure 6 gives the mean fields of polydispersity, short-chain branching (SCB), long-chain branching (LCB), and double bond (DB) frequencies inside the reactor for Case 1. The polydispersity, which is the ratio of weight-average to number-average molecular weight, along with branching characteristics govern the molecular properties such as melt flow index of the final polymer. The top left of Figure 6 shows a unit value of polydispersity close to the inlet of the reactor. However, occurrence of numerous chain-transfer reactions coupled with varying kinetic rates in the poorly mixed region produces shorter polymer chains, thereby increasing the polydispersity to 3.2 at the outlet of the reactor. This indicates that the breadth of molecular weight distribution increases along the length of the reactor, which produces a polymer product with nonuniform polymer properties. This phenomenon also affects the frequency and type of chain branching (SCB vs. LCB) as well as occurrence of DB in the final product (see Figure 6). The increase in SCB decreases polymer density along the length of the reactor, whereas the increase in LCB affects other rheological properties such as melt flow index. Thus, the detailed information about the molecular characteristics of the final polymer produced under various operating and mixing conditions can be used as a rudimentary guide to produce higher-quality products for appropriate end use.

Studies were carried out for other operating conditions (such as g_I, Q_I, and C_ϕ). The species and temperature profiles for these parameters showed trends that were similar to those in Figures 5 and 6 under extreme mixing conditions and hence, the detailed surface plot for other conditions are not reported herein.

Global ethylene decomposition

We can extract interesting and useful information regarding global decomposition events from the transported PDF simulations. Figure 7 shows the mean temperature and mean initiator mass fraction surface plots using I-3 for Cases 1 and 2, with $g_I = 6.575 \times 10^{-5}$ and $p_{1,0} = 6.25\%$. The various physical and thermodynamical constants as well as initial conditions used in the simulation are the same as those used in Figure 5. The transported PDF simulation for Case 1 shows that the mean temperature field increases from the initial value to a new steady state at 350°C, indicating the safe operation. However, for Case 2, the imperfect mixing between highly concentrated initiator and monomer creates very high radial initiator concentration gradients (see right column of Figure 7). This causes rapid burnout of initiator for Case 2 and it is consumed right near the injection point. This increases the localized temperature and starts local decomposition of ethylene, which creates large temperature fluctuations crossing the threshold required for ethylene decomposition. This occurrence of local hot spots will start local decomposition of ethylene,

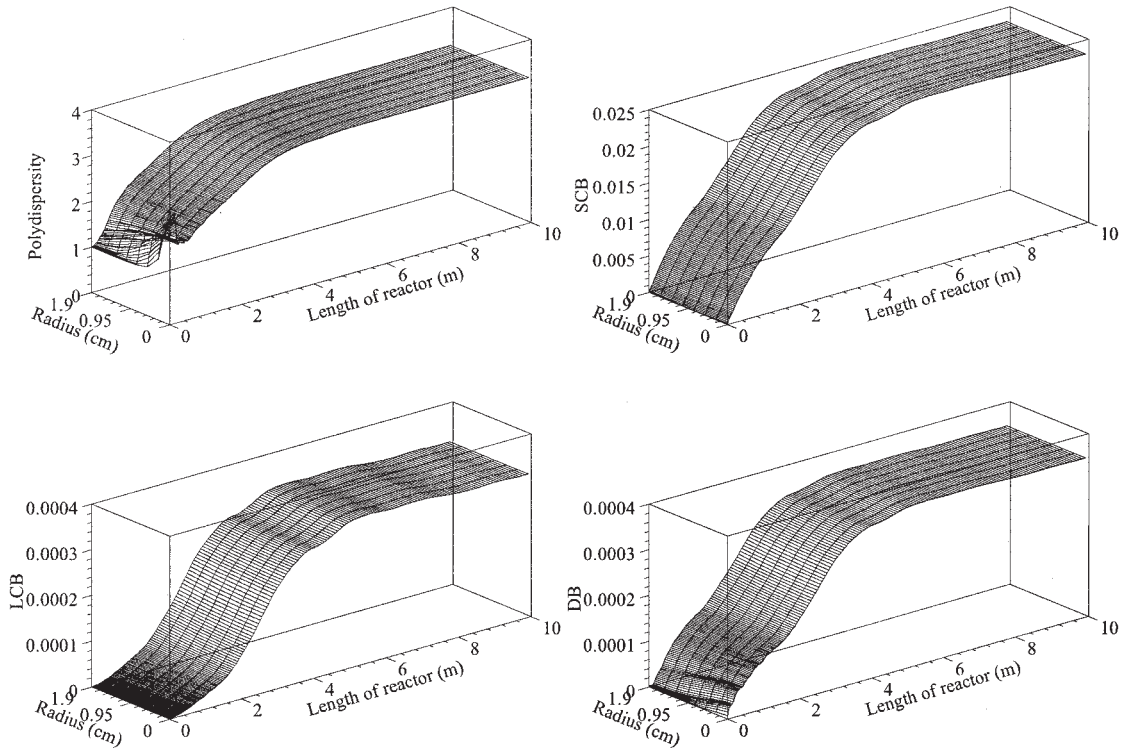

Figure 6. Time-averaged surface plots for polydispersity (top left), SCB (top right), LCB (bottom left), and DB (bottom right) mean fields in the computational domain for Case 1.

which will eventually lead to global decomposition increasing the temperature to the steady-state decomposition temperature (see left column of Figure 7). A change in T_{feed} from 225 to 250°C thus dramatically alters the reactor performance from steady operation to global decomposition. Figure 8 shows the corresponding surface plots for the mean monomer and initiator mass fraction fields for Cases 1 and 2. The occurrence of global decomposition for Case 2 marks the sudden consumption of the entire monomer volume over short time scales and monomer conversion increases from 10% for Case 1 to 100% for Case 2 (see left column of Figure 8). The right column of Figure 8 shows that the carbon mass fraction increases from 0.04% for Case 1 to almost 40% for Case 2. Thus the global decomposition causes release of a high volume of small decomposition products (C, CH_4, C_2H_2, and C_2H_6), which results in sudden development of pressure and temperature leading to runaway conditions.

Reactor stability analysis

Transported PDF simulations are carried out for different values of g_I at $p_{1,0}$ = 6.25, 14.06, and 25.0% (corresponding to two, three, and four injection cells for the initiator stream) to analyze the stability of the reactor. The results are summarized in a reactor stability map (see Figure 9), which is obtained by plotting g_I vs. the minimum volume fraction of environment 1 at the inlet ($p_{1,0}$). The map gives the maximum limit on g_I corresponding to a particular value of $p_{1,0}$, that is, with ring-mode injection of initiator I-2 ($p_{1,0}$ = 10%), safe operation of the reactor is ensured if the initiator mass fraction is less than or equal to approximately 4×10^{-4} (found using the solid line in Figure 9). Thus, the shaded part of the figure and the circle symbols indicate reactor "decomposition" or global reactor runaway. As the extent of premixing between initiator and monomer (that is, $p_{1,0}$) increases, the possibility of reactor runaway decreases and the reactor gives plug-flow performance after $p_{1,0}$ = 50%. The unshaded area and the cross symbols (see Figure 9) indicate stable reactor operation. High T_{feed} values (for example, 250°C) yield very low operating limits for g_I. The stability curve moves in a positive or negative direction along the *y*-axis, depending on the higher or lower T_{feed} values. The operating parameters must be chosen in the stable region to control the final product quality while considering the interaction between micromixing and all the possible polymerization kinetic steps including ethylene decomposition. Thus, plots such as Figure 9 are helpful in avoiding global reactor runaway arising from mixing effects while controlling the reactor productivity and the product quality. The impressive capability of the transported PDF approach to predict complex turbulence–chemistry interactions provides us insights into the reactor operation for conditions that are beyond available experimental facilities. It thus offers a particularly low-cost alternative for studying the dynamics of reactors near critical points of operation where instabilities occur.

Effect of initiator feed pulsation

The study was further extended to investigate the effect of initiator feed pulsation occurring in industrial reactors. Transported PDF simulations are carried out using initiator I-2 for Case 1, $g_I = 1.11 \times 10^{-4}$ and $p_{1,0}$ = 6.25%. Case 1 was selected because it showed safe operation for the reactor under

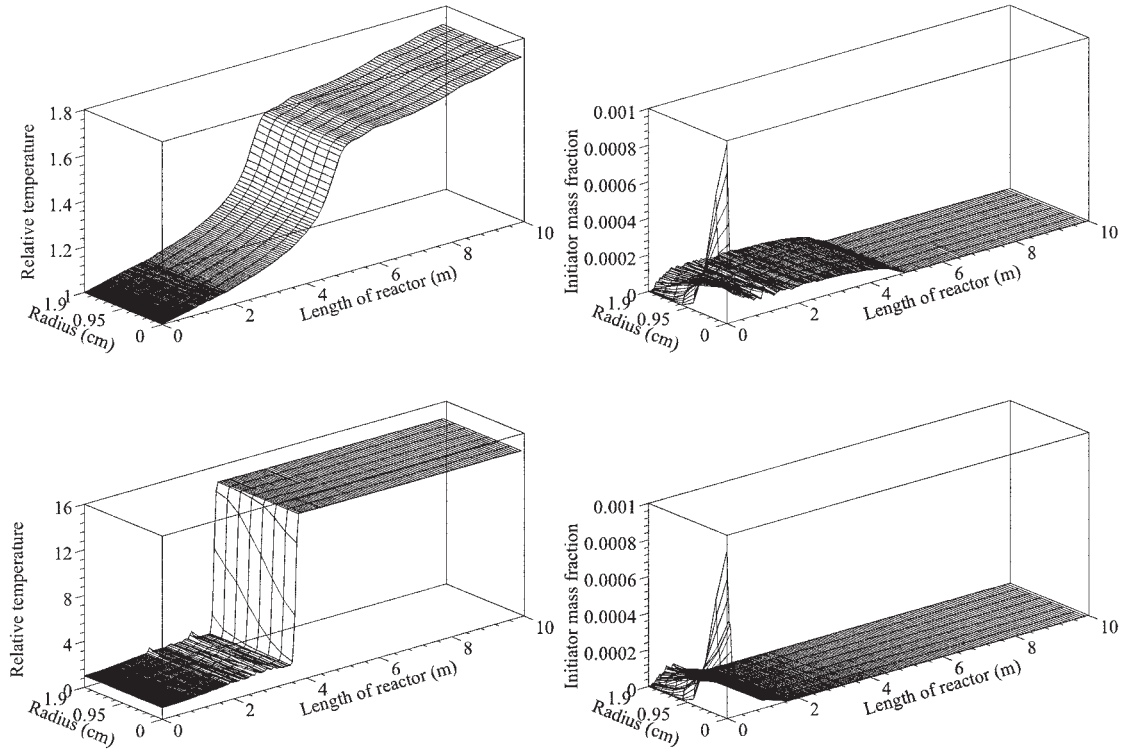

Figure 7. Prediction of global decomposition using transported PDF simulation for time-averaged relative temperature (left column) and g_I (right column) surface plots using initiator I-3 at C_Φ = 1.0, center-mode initiator injection ($p_{1,0}$ = 6.25%), and $g_{I,0} = 6.575 \times 10^{-5}$.

Case 1 for top surface plots; Case 2 for bottom surface plots.

non-pulsating conditions. However, it is still vulnerable to slight changes in feed conditions because of its proximity to the safety limits of reactor stability. The initiator feed pulsation is obtained by injecting initiator for one time step in every ten time steps with pulsating amplitude ten times higher than that of non-pulsating feed (that is, with the same time-averaged mass flow rate). In the remaining nine time steps in the pulsating cycle, cold monomer is injected. The plant-scale reactor is simulated for the whole pulsating cycle with a frequency of 260 Hz.

Figure 10 shows the surface plots for the time-averaged mean fields of initiator mass fraction and temperature with continuous and pulsed feed of I-2 initiator for Case 1. As discussed before, the poor micromixing between chemical species creates a large concentration gradients in the initiator field near the injection point, leading to non-uniform consumption of initiator and varying polymerization rates. The concentration fluctuations are intensified when initiator feed pulsation occurs. The highly concentrated initiator pulses, coupled with poor mixing resulting from center-mode injection, causes a more than two-fold increase in the magnitude of the concentration fluctuations. As a result, initiator burns out more rapidly and the length over which the initiators get completely consumed decreases from 5 to 1.5 m.

The temperature fields in Figure 10 record the corresponding increases from the initial value to a new steady state for the continuous feed for Case 1. However, with feed pulsation, highly concentrated initiator pulses create temperature pulses in the reaction mixture near the injection point. Initially, these pulses are relatively small and exist only on a local scale. When the local temperature exceeds 350°C, local decomposition of ethylene will cause higher temperature pulses that will eventually lead to global decomposition, increasing the temperature to the steady-state decomposition temperature. The initiator feed pulse coupled with the poor mixing further intensified the temperature fluctuations, thereby dramatically increasing the risk of global decomposition. Thus the initiator feed pulsation magnifies the adverse effect of poor mixing and gives a performance similar to that of higher feed temperatures with continuous feed. It is thus concluded that initiator feed pulsation can significantly lower the maximum operating limit of the monomer feed temperature.

Fundamental microscale flow information

In addition to global decomposition, the transported PDF method is also able to describe local hot spots occurring inside the reactor. The information is obtained by analyzing scatter plots of temperature along the length of the reactor in the poorly mixed region. Typically, for fully developed turbulent pipe flow, the poorly mixed region is defined by the length of the reactor equal to 50 pipe diameters. In our case, this length is approximately 2 m.[7] Figure 11 shows the distribution of local hot spots and local decomposition events in the poorly mixed region using the transported PDF method. As seen in the scatter plot of temperature (bottom of Figure 11), the temperature in the poorly mixed region follows a bi-level distribution, one mode corresponding to the injection environment and the other

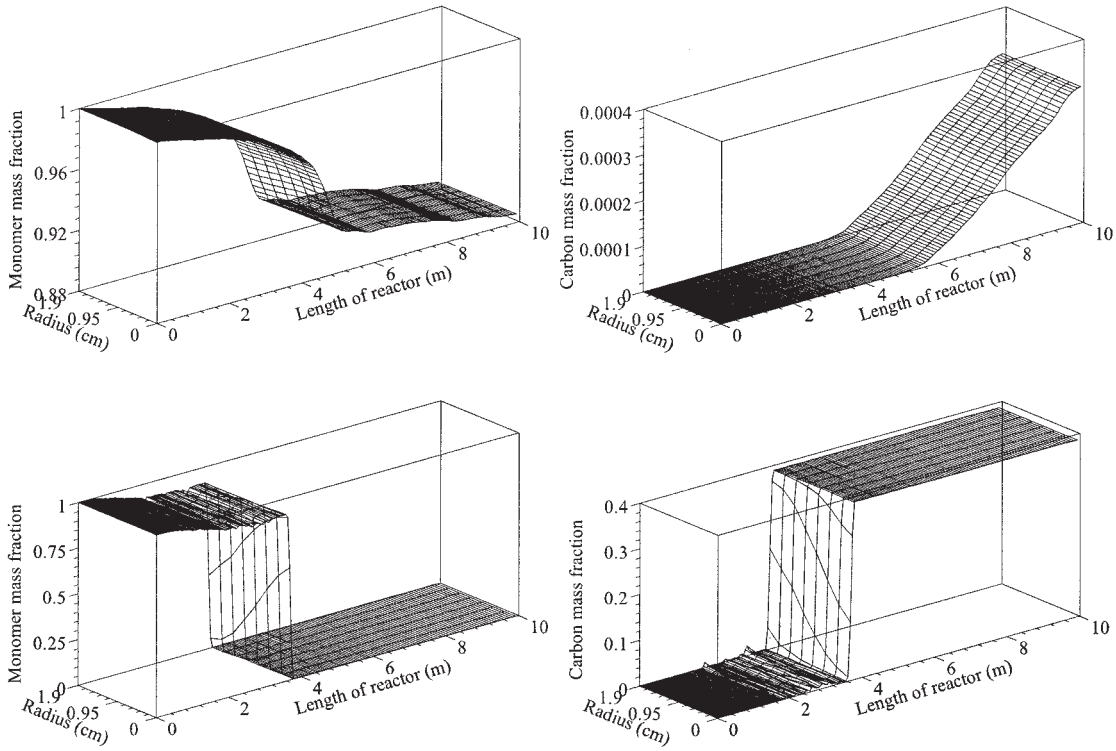

Figure 8. Prediction of global decomposition using transported PDF simulation for time-averaged g_M (left column) and g_C (right column) surface plots using initiator I-3 at C_ϕ = 1.0, center-mode initiator injection ($p_{1,0}$ = 6.25%), and $g_{I,0} = 6.575 \times 10^{-5}$.

Case 1 for top surface plots; Case 2 for bottom surface plots.

corresponding to the coflow environment, which nearly matches the radially-averaged temperature (indicated by the thick line). The poorly mixed initiator gives a high local concentration of initiator near the initiator injection point, giving high polymerization rates in some fluid particles. This increases the temperature above the average values giving local hot spots in the poorly mixed region.

This phenomenon is particularly significant in the plant-scale reactor where a mixture of low- and high-temperature initiators is used. The high-temperature initiator gets activated at the local hot spots, further increasing the temperature. This causes large temperature fluctuations about the mean values. The ethylene decomposition is favored when temperature fluctuations cross the threshold temperature (about 350°C). From the top of Figure 11 we see that local decomposition occurs when some hot spots are observed at about 1.75 m. The occurrence

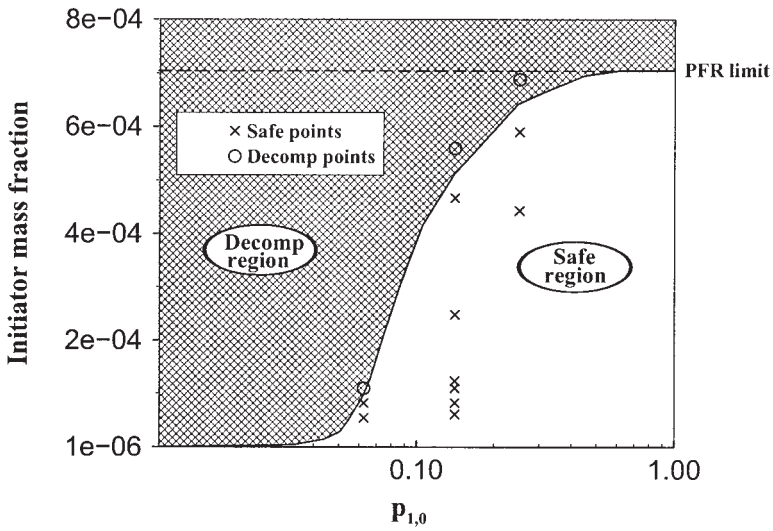

Figure 9. Reactor stability map using transported PDF simulation for initiator I-2 for Case 2.

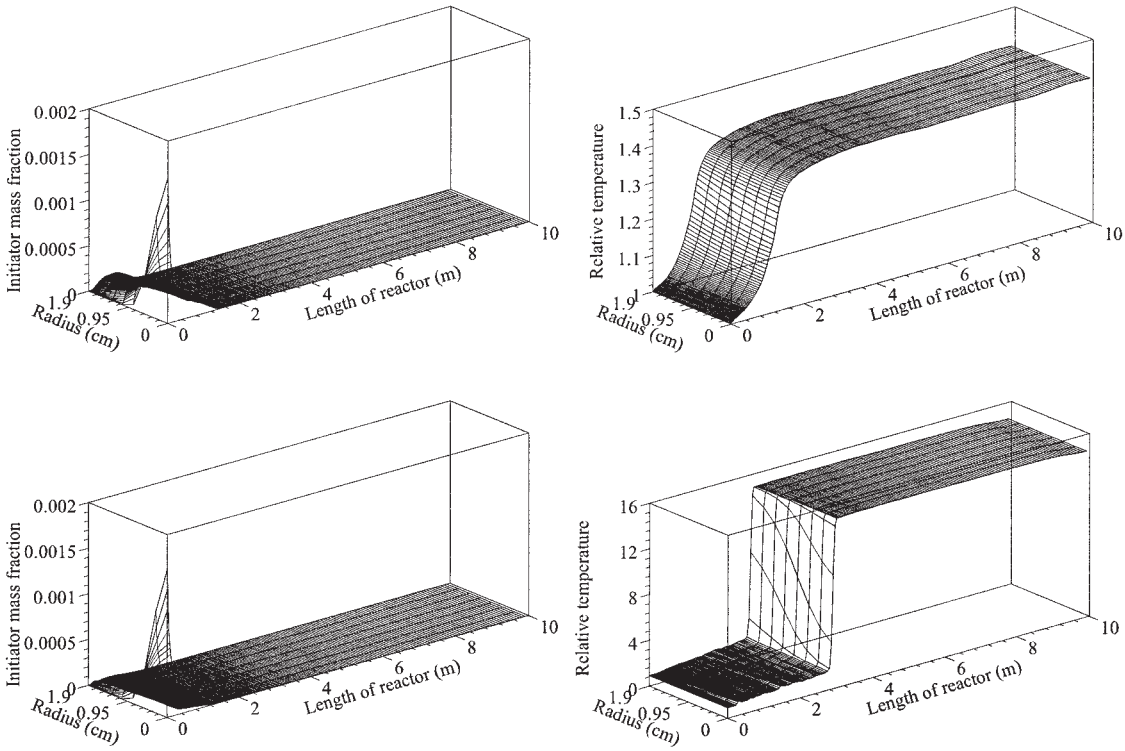

Figure 10. Prediction of global decomposition for pulsed initiator feed using transported PDF method for initiator I-2 with C_ϕ = 1.0, Case 1, and $p_{1,0}$ = 6.25%.

Top: no pulse; bottom: pulse.

of local decomposition does not affect the average temperature in the poorly mixed region. However, it has a significant effect on the performance of the reactor after radial mixing is complete. The local decomposition in the poorly mixed region coupled with the induction time required for global decomposition increases the temperature of the reactor to the steady-state decomposition temperature at about 4 m in the radially homogeneous region. From the standpoint of reactor control, these results indicate that it may be possible to detect local decomposition events and to apply extinction strategies before global decomposition occurs.

The detailed investigation of simulations at other operating conditions using temperature scatter plots provides further insights into the decomposition phenomenon. Figure 12 shows the distribution of local hot spots in the poorly mixed region using the transported PDF simulation at $C_\phi = 1.0$ for Case 2. As seen in the scatter plots, the PDF of temperature in the poorly mixed region again follows a bi-level distribution. The temperature range of the hot spots increases with the increase in g_I from 5.55×10^{-5} to 8.33×10^{-5} at $p_{1,0} = 6.25\%$ (top of figure) and finally causes global decomposition when g_I reaches a critical value of 1.11×10^{-4} (bottom left). However, with slightly better premixing ($p_{1,0} = 14.06\%$), the global decomposition is avoided completely (bottom right).

Finally, Figure 13 shows scatter plots of carbon mass fraction vs. T_{feed} for different values of g_I and $p_{1,0}$. At $g_I = 8.33 \times 10^{-5}$ and 14.06% premixing (top), the negligible carbon mass fraction indicates no local decomposition. However, with a decrease in premixing to 6.25%, local decomposition starts at $g_I = 8.33 \times 10^{-5}$. Individual particles show the production of carbon locally when the temperature exceeds ~350°C and these particles come back to the mean value as the result of mixing at the later part of the reactor (bottom). Thus it is concluded that the critical temperature required for occurrence of decomposition events in the tubular reactor is ~350°C. The generally accepted temperature for autoclaves is 300°C.[31,32,41] The higher value for tubular reactors may be attributed to the lower temperatures of the reaction mixture close to the initiator injection point, whereas in autoclaves the initiator is injected into a well-mixed reaction mixture with temperature nearly equal to the outlet temperature.

Validation of presumed PDF methods

Presumed PDF (P-PDF) methods take into account the key mixing phenomenon in the tubular reactor as well as the complex ethylene polymerization and decomposition kinetics, but neglect turbulent diffusivity. It was shown that a simplified P-PDF approach [multi-environment micromixing (MEM) model] is a very useful tool for creating reactor stability maps to predict regions of local and global decomposition as well as to evolve design strategies for stable reactor operation.[7] The important capability of the MEM model lies with its strength to provide detailed quantification of the initiator loss under various industrial operating parameters.[6,42] However, there is a need to validate these predictions using the more accurate and detailed transported PDF approach as a final check-up for the chosen set of operating conditions. Here, the axial profiles of the radially-averaged species and temperature from the trans-

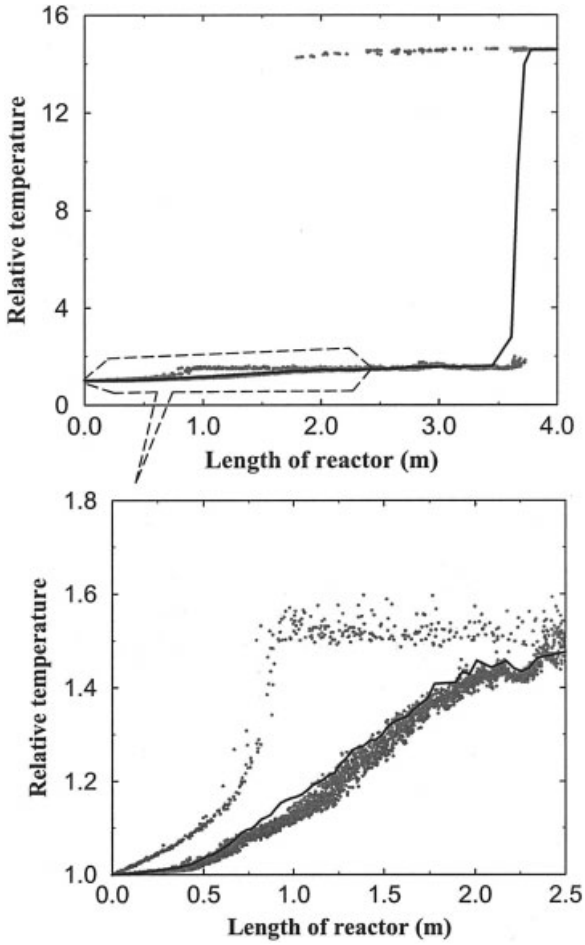

Figure 11. Bi-level distribution of relative temperature scatter plot in the poorly micromixed region using transported PDF method for Case 2 with C_ϕ = 1.0 and $p_{1,0}$ = 6.25%.

Solid line: mean relative temperature; points: particle relative temperatures.

ported PDF simulation are used to validate the MEM simulations.

The turbulent mixing parameter C_ϕ, which is defined as the ratio of scalar mixing time to the inertial mixing time, lumps together the effect of molecular and turbulent diffusion processes in the MEM model. However, transported PDF methods use a gradient-diffusion model to account for the turbulent diffusion separately. Another crucial parameter, $p_{1,0}$, which decides the extent of premixing, has a significant effect on the scalar-variance distribution in both models. Thus the flow physics associated with scalar mixing must be validated for different initial mixing conditions after omitting chemical source terms. To make a meaningful comparison between the MEM and transported PDF simulations for scalar mixing, the moments (mean and variance) of a non-reacting species from the two approaches are matched by varying the mixing parameters C_ϕ and $p_{1,0}$.

The mean ($\langle\xi\rangle_R$) and variance ($\langle\xi'^2\rangle_R$) of initiator mass fraction are computed by radially averaging the transported PDF simulations without chemical source term with C_ϕ = 1.0 and $p_{1,0}$ = 6.25% (corresponding to two injection cells for the initiator stream). The profiles are compared with the MEM predictions using $p_{1,0}$ values of 0.0625 and 0.0935 at C_ϕ = 1.0 in Figure 14. The values of mean and variance of ξ agree almost exactly for $p_{1,0}$ = 0.0935. Thus the MEM predictions are made more realistic by adjusting the values of $p_{1,0}$ to account for the simplified fluid mechanics. The predictions are also investigated for different values of C_ϕ at $p_{1,0}$ = 0.0935 by comparing the intensities of the segregation profiles in the poorly mixed region. The intensity of segregation (I_s) indicates the degree of mixing (for example, I_s = 1 for a completely segregated system and I_s = 0 for a perfectly micromixed system) and is defined as

$$I_s = \frac{\langle\xi'^2\rangle_R}{\langle\xi\rangle_R(1-\langle\xi\rangle_R)} \tag{17}$$

The radially-averaged profiles of the intensity of segregation are obtained using the MEM predictions for C_ϕ values of 0.5, 1.0, and 2.0, and are compared with the transported PDF predictions for C_ϕ = 1.0 in Figure 15. The excellent agreement for intensity of segregation for C_ϕ value of 1.0 indicates that C_ϕ is the same in both models. Thus, lack of turbulent diffusivity in the MEM model must be accounted for by increasing $p_{1,0}$, that is, degree of premixing. The increased $p_{1,0}$ values in the MEM model [$(p_{1,0})_{MEM}$] are computed using the same procedure for different numbers of initiator injection cells [$(p_{1,0})_{PDF}$] in the transported PDF simulations and are summarized in Figure 16.

Figures 17 and 18 show the comparison of the axial profiles of the radially-averaged initiator consumption, monomer conversion, temperature, and LCB frequency. The triangular symbols indicate identical simulation conditions for the two PDF method using Case 1 with C_ϕ = 1. As seen in the top part of Figure 17, the MEM model predicts sudden burnout of initiator close to the injection point. At $p_{1,0}$ = 0.0625 and C_ϕ = 1, the MEM model simulations exhibit unrealistic consumption of initiator and local decomposition of ethylene in the injection environment. As discussed above, this behavior is attributed in part to underestimation of the degree of premixing (that is, 0.0625 vs. 0.0935). The corresponding profiles of monomer conversion, temperature, and LCB frequency are shown in the bottom part of Figure 17, top part of Figure 18, and bottom part of Figure 18, respectively.

The usefulness of the presumed PDF to study reactor stability maps and initiator efficiency profiles further tempts us to make the model predictions more realistic by incorporating the higher values of $p_{1,0}$ obtained from Figure 16. The circles in Figures 17 and 18 indicate the MEM predictions with $p_{1,0}$ = 0.0935 and C_ϕ = 1. The local decomposition of ethylene is now completely avoided by increased premixing at the inlet. However, the results are still unrealistic because of the overly simple shape of the presumed PDF. In the case of reacting scalars, the effective turbulent diffusivity is lower than that for the non-reacting case. The mixing parameter C_ϕ, which accounts for both molecular mixing and turbulent diffusivity in the MEM model, must be lowered to a value of 0.63 to account for this change in radial mixing arising from the reaction. At this value of C_ϕ, MEM model predictions (Figures 17 and 18) more closely match with transported PDF simulations. With this increased accuracy of the predictions, the MEM model will

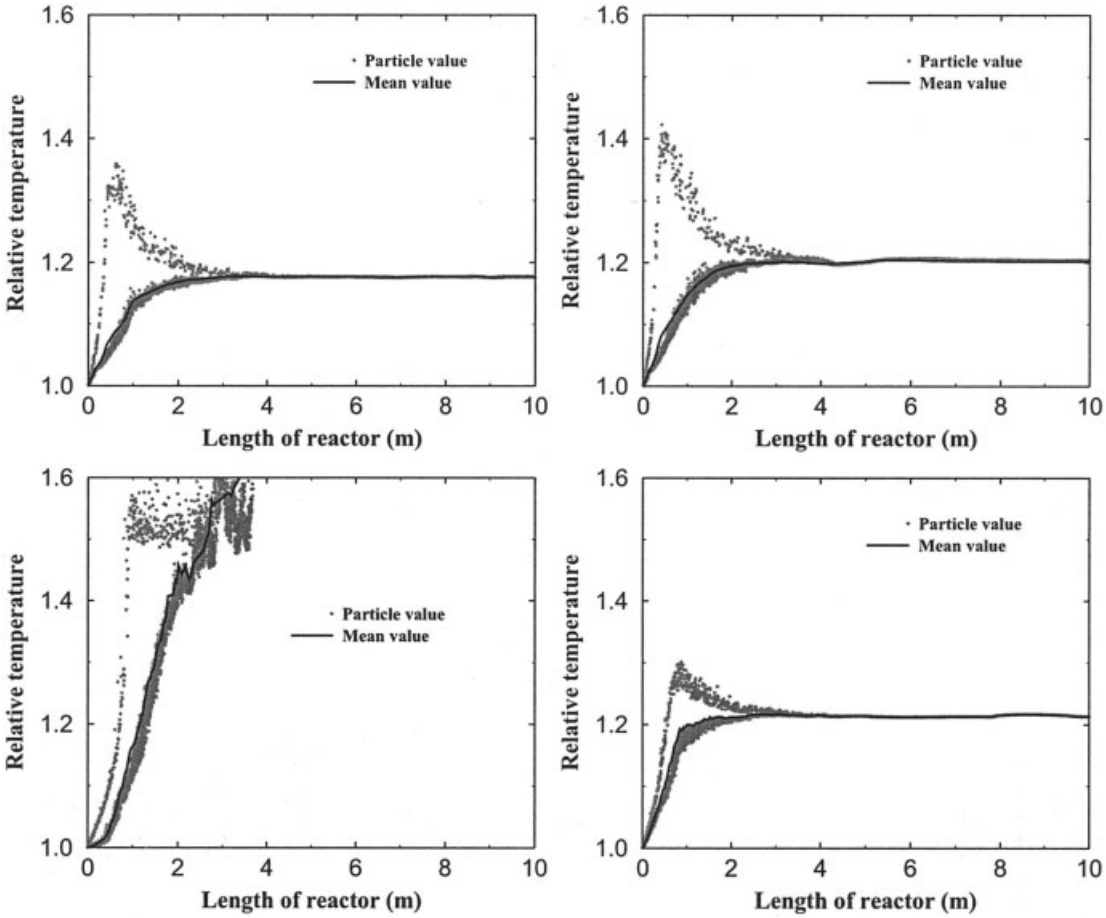

Figure 12. Distribution of local hot spots in the computational domain using transported PDF method with $C_\phi = 1.0$ for Case 2.

Top left: $g_{I,0} = 5.55 \times 10^{-5}$ and $p_{1,0} = 6.25\%$; top right: $g_{I,0} = 8.33 \times 10^{-5}$ and $p_{1,0} = 6.25\%$; bottom left: $g_{I,0} = 1.11 \times 10^{-4}$ and $p_{1,0} = 6.25\%$; bottom right: $g_{I,0} = 1.11 \times 10^{-4}$ and $p_{1,0} = 14.06\%$.

be very helpful in studying the effect of micromixing on reactor stability and initiator efficiency for various sets of process operating conditions with extremely low computational cost.

Conclusions

A state-of-the-art transported PDF method was used to study mixing between initiator and monomer inside a plant-scale tubular LDPE reactor. It was shown that poor mixing can result in unstable reactor operations and loss of expensive initiators under the extreme process conditions that are used to maximize conversion in industrial practice. The transported PDF method incorporated turbulent diffusivity as well as the effect of micromixing on the species consumption, and represented the chemical source terms exactly without any closure approximations. The large number of variables and stiff chemistry calculations for each particle at each iteration led to relatively high CPU times for unsteady-state transported PDF simulations. However, the implementation of ISAT allowed us to tackle the formidable task of implementing comprehensive LDPE chemistry in the transported PDF simulations. The flow information obtained from the simulations increased our understanding of turbulent reacting mixing in the LDPE polymerization process. It helped us to quantify the strong coupling between micromixing and the local as well as global decomposition conditions, and provided fundamental knowledge needed to make wiser and well-informed design decisions. Overall, this study has brought turbulent reacting flow simulation for single-phase finite-rate chemistry closer to realistic chemical process engineering applications.

The transported PDF simulations predicted an adverse effect of mixing on monomer conversion (that is, yield), initiator consumption (that is, efficiency of the process), polydispersity, and molecular characteristics of the final polymer (that is, selectivity) for various mixing and operating conditions such as initiator concentration, initiator flow rate (degree of premixing), feed temperature, and the pulsating feed of the initiator. The importance of temperature fluctuations (local hot spots) was realized when dealing with ethylene decomposition chemistry. Interesting features such as a bi-level temperature distribution and global decomposition after induction time were also observed under certain conditions (for example, Case 2 with $g_I = 1.11 \times 10^{-4}$ and $p_{1,0} = 0.0625$) using the transported PDF simulations near critical points, where instabilities occur. This information can be effectively summarized in reactor stability maps, which are extremely helpful in the design of operational strategies to avoid global runaway conditions while selecting

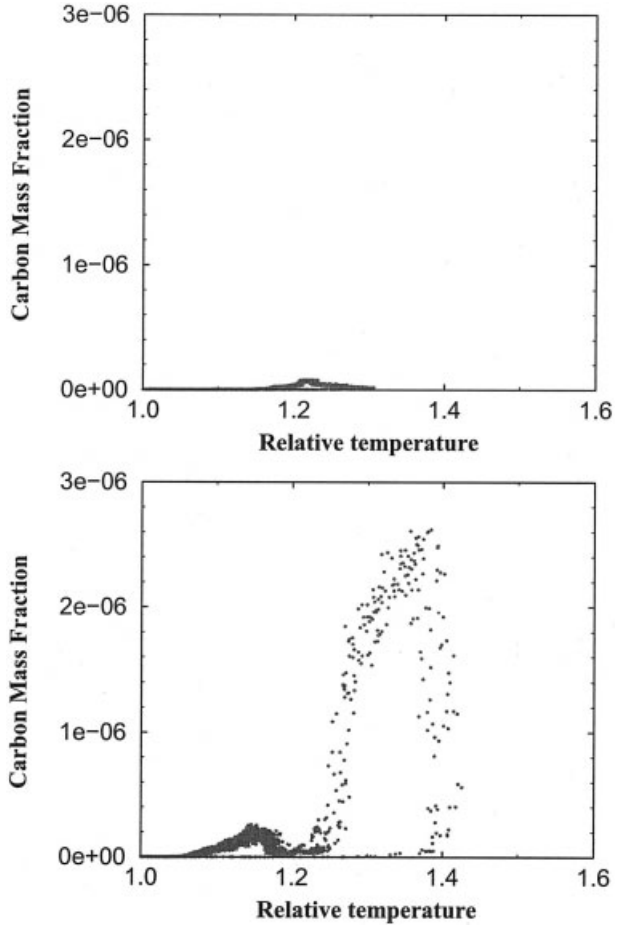

Figure 13. Distribution of local decomposition in the computational domain using transported PDF method with C_ϕ = 1.0 for Case 2.

Top figure is simulated at $g_I = 8.33 \times 10^{-5}$ and $p_{1,0} = 14.06\%$, whereas bottom figure is simulated at $g_I = 8.33 \times 10^{-5}$ and $p_{1,0} = 6.25\%$.

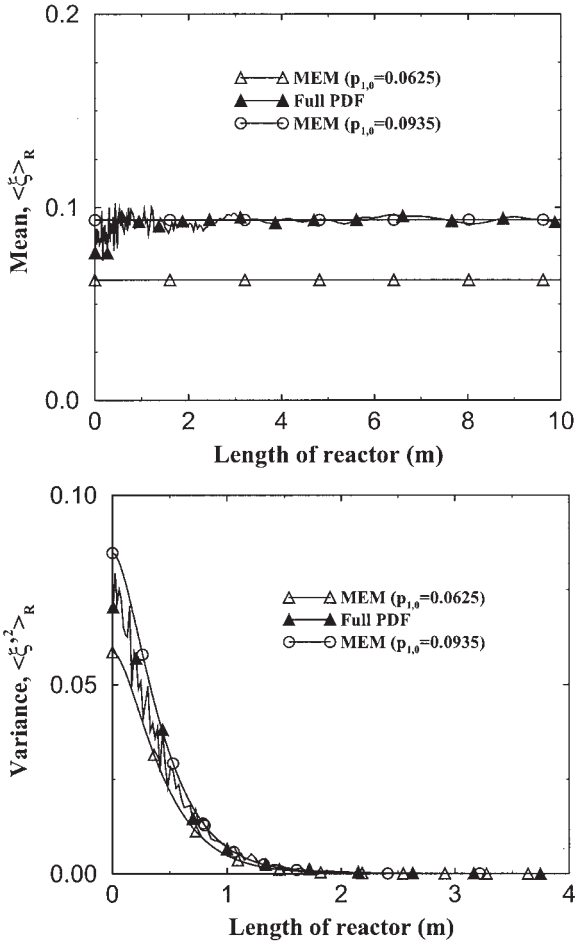

Figure 14. Comparison of the MEM predictions with transported PDF simulations for the mean and variance of a non-reacting scalar (ξ) with C_ϕ > = 1.

The variance at the inlet of the reactor is given as: $\langle\xi'^2\rangle_R(0) = p_{1,0}(1 - p_{1,0})$.

optimal operating parameters in the safe region. The initiator feed pulse, coupled with poor micromixing, further intensified the temperature fluctuations, thereby dramatically increasing the risk of global decomposition or decreasing the maximum limits of the monomer feed temperature. The investigation of local decomposition events under various operating conditions led to the conclusion that there is increased risk of decomposition near 350°C. The high crossover temperature, compared to 300°C for autoclaves, could be attributed to the fact that the temperature in the initiator injection region inside the tubular reactor is lower than that of autoclaves.

Finally, the accuracy and efficiency of MEM model were validated against the detailed transported PDF simulations using the same kinetics and operating conditions. Using the non-reacting scalar, it was found that the simplified fluid mechanics in the MEM model needs to be compensated for by increasing $p_{1,0}$ and by decreasing the turbulent mixing parameter C_ϕ to describe the effect of chemistry on the turbulent diffusivity. For example, $p_{1,0} = 0.0935$ with $C_\phi = 0.63$ in the MEM model simulated the LDPE reactor realistically as compared to $p_{1,0} = 0.0625$ with $C_\phi = 1.0$ in the transported PDF

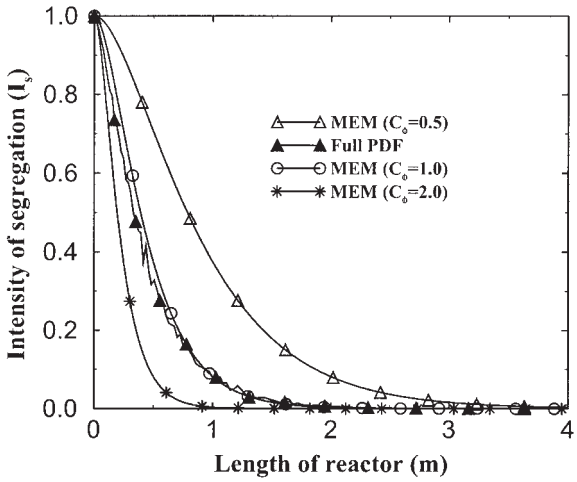

Figure 15. Comparison of the MEM predictions with transported PDF simulations for the intensity of segregation of a non-reacting scalar at $p_{1,0}$ = 0.0935.

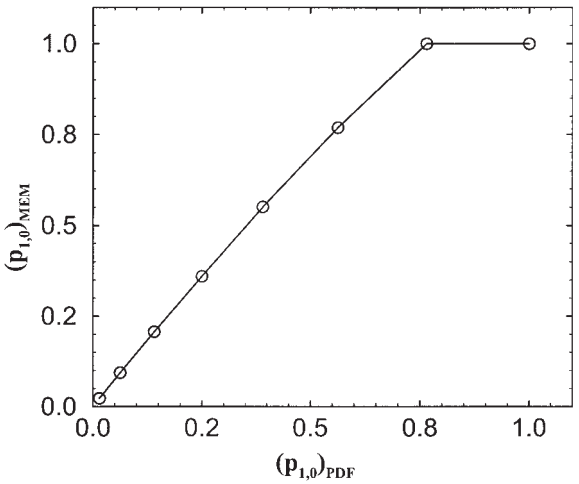

Figure 16. Comparison of $p_{1,0}$ predictions using the MEM and transported PDF models.

method. Moreover, the MEM model is computationally highly efficient: it took approximately 1 min of CPU time compared to 24 h required for the transported PDF approach on a Sun Ultra

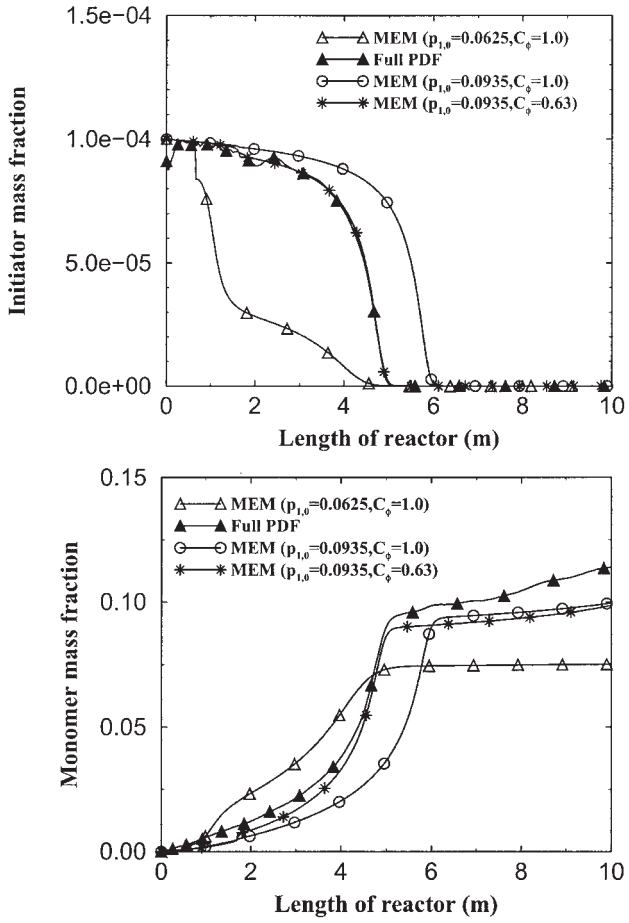

Figure 17. Comparison of the MEM predictions with transported PDF simulations for radially-averaged profiles of initiator and monomer mass fractions for Case 1.

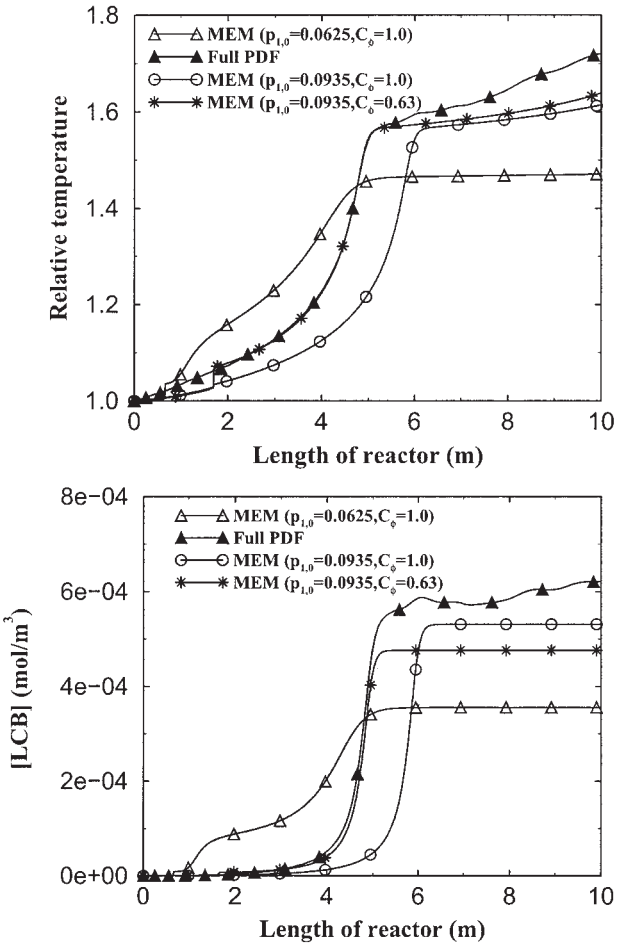

Figure 18. Comparison of the MEM predictions with transported PDF simulations for radially-averaged profiles of relative temperature and frequency of LCB for Case 1.

80 workstation, and is thus extremely useful for studying reactor stability maps and initiator efficiency profiles under various mixing and operating conditions. Thus the two methods are largely complementary, each being able to capture and describe some of the important processes occurring on different flow scales. The integration of capabilities of the two methods provided important insights into the selection of optimal operating conditions while controlling the reactor stability and the product quality.

Acknowledgments

This work was supported by the National Science Foundation under Grant CTS-9996242, BASF AG, Germany, and Basell Polyolefine GmbH, Germany.

Notation

$\mathbf{C}$ = convection process arising from mean velocity, m/s
C_p = specific heat of reaction mixture, J kg^{-1} K^{-1}
C_ϕ = turbulent mixing parameter, dimensionless
$\mathbf{D}$ = turbulent diffusion process, m/s
D_α = molecular diffusivity, m^2/s
D_I = diameter of initiator injection nozzle, m
D_M = diameter of tubular reactor, m

E_a = activation energy of the generalized Arrhenius equation, m^3 mol^{-1} s^{-1}
f_{ni} = efficiency of ni^{th} initiator, dimensionless
f_ϕ = joint composition probability density function
g_C = carbon mass fraction, dimensionless
g_I = initiator mass fraction, dimensionless
g_M = monomer mass fraction, dimensionless
k = turbulent kinetic energy, m^2/s^2
k_0 = preexponential factor of the generalized Arrhenius equation, m^3 mol^{-1} s^{-1}
k_1 = rate constant for initiation in decomposition, m^3 mol^{-1} s^{-1}
k_6 = rate constant for propagation in decomposition, , m^3 mol^{-1} s^{-1}
k_{cta} = rate constant for chain transfer to CTA, m^3 mol^{-1} s^{-1}
k_{d_I} = rate constant for initiator dissociation, 1/s
k_I = rate constant for initiation in polymerization, m^3 mol^{-1} s^{-1}
k_{LCB} = rate constant for formation of long-chain branches, m^3 mol^{-1} s^{-1}
k_p = rate constant for propagation in polymerization, m^3 mol^{-1} s^{-1}
k_{SCB} = rate constant for backbiting, m^3 mol^{-1} s^{-1}
k_t = rate constant for termination in decomposition, m^3 mol^{-1} s^{-1}
k_{tc} = rate constant for termination by combination, m^3 mol^{-1} s^{-1}
k_{td} = rate constant for termination by disproportionation, m^3 mol^{-1} s^{-1}
k_{trm} = rate constant for chain transfer to monomer, m^3 mol^{-1} s^{-1}
k_{trp} = rate constant for chain transfer to polymer, m^3 mol^{-1} s^{-1}
k_β = rate constant for β-scission, m^3 mol^{-1} s^{-1}
$\mathbf{M}$ = molecular mixing process, mol m^{-3} s^{-1} or K/s
$p_{1,0}$ = volume fraction of environment 1 at the injection point, dimensionless
P_{atm} = pressure inside the tubular reactor, atm
Q = volumetric flow rate, m^3/s
R = ideal gas constant, cm^3 atm^{-1} mol^{-1} K^{-1}
$\mathbf{S}$ = chemistry process, mol m^{-3} s^{-1}
S_α = chemical source term, mol m^{-3} s^{-1}
s = integration variable
t = time, s
T_{avg} = average temperature of the reaction mixture, K
T_{feed} = monomer feed temperature, K
u_i = turbulence intensity, m/s
$\langle U_i \rangle$ = average mean velocity in the ith direction, m/s
U_i = velocity in the ith direction, m/s
V_a = activation volume of the generalized Arrhenius equation, cm^3/mol
v = axial velocity, m/s
x_i = length in the ith direction, m
x = length vector, m

Greek letters

ΔH_{decomp} = heat of ethylene decomposition, J/mol
ΔH_{poly} = heat of polymerization, J/mol
Δt = time step, s
ε = turbulent dissipation rate, m^2/s^3
ε_{tol} = user-supplied error tolerance in ISAT algorithm
λ_n = n-order moment of dead polymers
μ_n = n-order moment of free radicals
ω_n = n-order moment of secondary free radicals
ρ = density of reaction mixture, kg/m^3
τ_u = integral timescale, s
τ_ϕ = micromixing timescale, s
$\boldsymbol{\phi}$ = composition vector, mol/m^3
ϕ_α = composition variable (species α or T), mol/m^3 or K
$\langle \phi_\alpha \rangle$ = mean composition variable, mol/m^3 or K
$\boldsymbol{\psi}$ = composition space vector, mol/m^3
ψ_α = composition space for variable α, mol/m^3 or K
$\boldsymbol{\xi}$ = standardized joint normal random vector
ξ = mixture fraction, dimensionless

Subscripts and superscripts

A = initiator free radical
DB = double bonds
I-1 = low-temperature initiator
I-2 = medium-temperature initiator
I-3 = high-temperature initiator
i = chain length of either free radicals or dead polymers
j = chain length of either free radicals or dead polymers
(j) = jth notional particle
LCB = long-chain branches
M = monomer
n_i = total number of initiators used in the chemistry
MEM = values for the multienvironment micromixing model
P = dead polymer chains
PDF = values for the transported PDF method
R = free-radical chains
R′ = secondary free-radical chains
SCB = short-chain branches
α = chemical species α or temperature T

Literature Cited

1. Raman V, Fox RO, Harvey AD, West DH. Effect of feed-stream configuration on gas-phase chlorination reactor performance. *Ind. Eng. Chem Res.* 2003;42:2544-2556.
2. Raman V, Fox RO, Harvey AD, West DH. CFD analysis of premixed methane chlorination reactors with detailed chemistry. *Ind. Eng. Chem. Res.* 2001;40:1-7.
3. Shah JJ, Fox RO. Computational fluid dynamics simulation of chemical reactors: Application of in-situ adaptive tabulation to methane thermochlorination chemistry. *Ind. Eng. Chem. Res.* 1999;38:4200-4212.
4. Sahgalov YA, Minsker KS, Zaikov GE. *Polymers Derived from Isobutylene: Synthesis, Properties, Application.* Boston, MA: Brill Academic Publishers; 2001.
5. Marcarian K, Falk L, Pla F, Villermaux J, Mueller AHE. Effect of micromixing in the continuous anionic polymerization of methyl methacrylate. *DECHEMA Monogr.* 1998;134:577-586.
6. Kolhapure NH, Fox RO. CFD in polymer reaction engineering: Combining polymerization chemistry and detailed flow models. *DECHEMA Monogr.* 2001;137:247-271.
7. Kolhapure NH, Fox RO. CFD analysis of micromixing effects on polymerization in tubular low-density polyethylene reactors. *Chem. Eng. Sci.* 1999;54:3233-3242.
8. Tosun G, Bakker A. A study of macro segregation in low-density polyethylene autoclave reactors by computational fluid dynamic modeling. *Ind. Eng. Chem. Res.* 1997;36:296-305.
9. Tsai K, Fox RO. PDF modeling of turbulent mixing effects on initiator efficiency in a tubular LDPE reactor. *AIChE J.* 1996;42:2926-2940.
10. Zauner R, Jones AG. Mixing effects on product particle characteristics from semi-batch crystal precipitation. *Chem. Eng. Res. Des. Trans. IChemE Part A.* 2000;78:894-902.
11. Piton D, Fox RO, Marcant B. Simulation of fine particle formation by precipitation using computational fluid dynamics. *Can. J. Chem. Eng.* 2000;78:983-993.
12. Marchisio DL, Barresi AA, Fox RO. Simulation of turbulent precipitation in a semi-batch Taylor–Couette reactor using CFD. *AIChE J.* 2001;47:664-676.
13. Baldyga J, Bourne JR. *Turbulent Mixing and Chemical Reactions.* New York, NY: Wiley; 1999.
14. Ita PA. World polyethylene capacity in the year 2001: Expansions and projected utilization rates. *Proc. of 56th Ann. Tech. Conf.* Brookfield, CT: Plastic Engineering; 1998:2749-2753.
15. Kwag BG, Choi KY. Modeling of a multistage high-pressure ethylene polymerization reactor. *Chem. Eng. Sci.* 1994;49:4959-4969.
16. Daiβ A, Kolhapure NH, Fox RO, Mähling F-O. CFD-analysis of heat transfer and initiator mixing performance in LDPE high pressure tubular reactors. *Comput.-Aided Chem. Eng.* 2000;8:427-432.
17. Zhang SX, Read NK, Ray WH. Runaway phenomena in low-density polyethylene autoclave reactors. *AIChE J.* 1996;42:2911-2925.
18. Blavier L, Villermaux J. Free radical polymerization engineering. II: Modelling of homogeneous polymerization of styrene in a batch reactor: Influence of initiator. *Chem. Eng. Sci.* 1984;39:101-110.
19. Nauman EB. Mixing in polymer reactors. *J. Macromol. Sci. Rev. Macromol. Chem. Phys.* 1974;10:75-112.
20. Villermaux J, Blavier L. Free radical polymerization engineering I: A

new method for modeling free radical homogeneous polymerization reactions. *Chem. Eng. Sci.* 1984;39:87-99.
21. Pope SB. Computationally efficient implementation of combustion chemistry using *in situ* adaptive tabulation. *Combust. Theor. Model.* 1997;1:41-63.
22. Fox RO. On the relationship between Lagrangian micromixing models and computational fluid dynamics. *Chem. Eng. Process.* 1998;37:521-535.
23. Kolhapure NH, Fox RO. LDPE—Prediction of the polymer product quality and the performance of tubular reactors from CFD analysis. *Proc. of Topical Session on Polym. React. Eng. II* (*AIChE Spring National Meeting*). Paper 77a. New York, NY: American Institute of Chemical Engineering; 1999:1-14.
24. Fox RO. *Computational Models for Turbulent Reacting Flows.* Cambridge, UK: Cambridge Univ. Press; 2003.
25. Pope SB. PDF methods for turbulent reactive flows. *Proc. Energy Combust. Sci.* 1985;11:119-192.
26. Villermaux J, Devillon JC. Representation de la coalescence et de la redispersion des domaines de segregation dans un fluide par un modele d'interaction phenomenologique. *Proc. 2nd Int. Symp. on Chem. React. Eng.* New York, NY: Elsevier; 1972:1-13.
27. Pope SB. *Turbulent Flows.* New York, NY: Cambridge Univ. Press; 2000.
28. Tsai K, Fox RO. PDF simulation of a turbulent series-parallel reaction in an axisymmetic reactor. *Chem. Eng. Sci.* 1994;49:5141-5158.
29. Kiparissides C, Verros G, MacGregor JF. Mathematical modeling, optimization, and quality control of high-pressure ethylene polymerization reactors. *J. Macromol. Sci. Rev. Macromol. Chem. Phys.* 1993; C33:437-527.
30. Zabisky RCM, Chan WM, Gloor PE, Hamielec AE. A kinetic model for olefin polymerization in high-pressure tubular reactors: A review and update. *Polymer.* 1992;33:2243-2262.
31. Albert J. *Thermal Decomposition of Pressurized Ethylene: Influence of Comonomers.* PhD Thesis. Darmstadt, Germany: Technological Univ. of Darmstadt; 1998.
32. Albert J, Luft G. Runaway phenomena in the ethylene/vinylacetate copolymerization under high pressure. *Chem. Eng. Process.* 1998;37:55-59.
33. Hulburt HM, Katz S. Problems in particle technology: A statistical mechanical formulation. *Chem. Eng. Sci.* 1964;19:555-574.
34. Lorenzini P, Pons M, Villermaux J. Free-radical polymerization engineering III: Modelling homogeneous polymerization of ethylene: Mathematical model and new method for obtaining molecular-weight distribution. *Chem. Eng. Sci.* 1992;47:3969-3980.
35. Goto S, Yamamoto K, Furui S, Sugimoto M. Computer model for commercial high-pressure polyethylene reactor based on elementary reaction rates obtained experimentally. *Appl. Polym. Symp.* 1981;36:21-40.
36. Buback M, Sandmann J. Pressure and temperature dependence of the decomposition rate of aliphatic tert-butyl peroxyesters. *Z. Phys. Chem.* (*Munich*). 2000;214:583-607.
37. Buback M, Lendle H. The chemically initiated high-pressure polymerization of ethylene. *Makromol. Chem.* 1983;184:193-206.
38. Lee KH, Marano JP. Free-radical polymerization: Sensitivity of conversion and molecular weights to reactor conditions. *ACS Symp. Ser.* 1979;104:221-251.
39. Roekaerts D. Use of a Monte Carlo PDF method in a study of the influence of turbulent fluctuations on selectivity in a jet-stirred reactor. *Appl. Sci. Res.* 1991;48:271.
40. Lorenzini P, Pons M, Villermaux J. Free-radical polymerization engineering. IV: Modelling homogeneous polymerization of ethylene: Determination of model parameters and final adjustment of kinetic coefficients. *Chem. Eng. Sci.* 1992;47:3981-3988.
41. Zhang SX, Ray WH. Modeling of imperfect mixing and its effects on polymer properties. *AIChE J.* 1997;43:1265-1277.
42. Kolhapure NH. *Computational Fluid Dynamics for Design and Optimization of Tubular Low Density Polyethylene Reactors.* PhD Thesis. Ames, IA: Iowa State Univ.; 2001.

Manuscript received Nov. 13, 2003, revision received Jun. 24, 2004, and final revision received Aug. 11, 2004.